TAMPEREEN TEKNILLINEN YLIOPISTO
TAMPERE UNIVERSITY OF TECHNOLOGY

Jari Nikkinen

Sub-100 ps Light Sources Based on Q-Switched Microchip Lasers

Julkaisu 1511 • Publication 1511

Tampere 2017

Tampereen teknillinen yliopisto. Julkaisu 1511
Tampere University of Technology. Publication 1511

Jari Nikkinen

Sub-100 ps Light Sources Based on Q-Switched Microchip Lasers

Thesis for the degree of Doctor of Science in Technology to be presented with due permission for public examination and criticism in Festia Building, Auditorium Pieni sali 1, at Tampere University of Technology, on the 22nd of November 2017, at 12 noon.

Tampereen teknillinen yliopisto - Tampere University of Technology
Tampere 2017

Doctoral candidate: Jari Nikkinen, M.Sc.
Optoelectronics Research Centre
Faculty of Natural Sciences
Tampere University of Technology
Finland

Supervisor: Mircea Guina, Prof.
Optoelectronics Research Centre
Faculty of Natural Sciences
Tampere University of Technology
Finland

Instructor: Antti Härkönen, Ph.D.
Optoelectronics Research Centre
Faculty of Natural Sciences
Tampere University of Technology
Finland

Pre-examiners: Katia Gallo, Prof.
Department of Applied Physics
KTH Royal Institute of Technology
Sweden

Hanne Ludvigsen, Ph.D.
Department of Electronics and Nanoengineering
Aalto University
Finland

Opponent: Valdas Pasiskevicius, Prof.
Department of Applied Physics
KTH Royal Institute of Technology
Sweden

ISBN 978-952-15-4047-9 (printed)
ISBN 978-952-15-4058-5 (PDF)
ISSN 1459-2045

Abstract

Laser pulses are instrumental for a wide range of applications in advanced measurement and imaging techniques, such as time-gated Raman spectroscopy or fluorescent lifetime measurements. Key features for these applications are the relatively high peak power, high pulse energy, and a short pulse duration. To this end, the goal of the thesis has been to demonstrate novel light sources emitting optical pulses with sub-100 ps duration at UV, visible, and infrared wavelengths. The sub-100 ps optical pulse regime fills a gap between the more complex mode-locked lasers and typical Q-switched microchip lasers, which emit optical pulses with duration longer than 300 ps. In particular, key efforts were allocated to developing Nd:YVO_4 microchip lasers, emitting either at 1064 nm or 1342 nm, and employing semiconductor saturable absorber mirrors for passive Q-switching. The typical pulse duration was ∼100 ps at 1064 nm and ∼200 ps at 1342 nm. Typical repetition rate was in 100 – 500 kHz range corresponding to average powers of several mW. These laser pulses were amplified in compact Nd:YVO_4 amplifiers up to an average power of 1.3 W. Then nonlinear wavelengths conversion techniques were employed to expand the emission wavelength and also to attain further pulse shortening.

State-of-the-art results have been achieved on several fronts of research. First of all, in this work the first Q-switched microchip lasers based on GaInNAs semiconductor saturable absorber was developed. Using second harmonic generation, we have achieved leading values for average power, pulse energy, and pulse duration for emission at 671 nm, and 532 nm. Using third harmonic generation we demonstrated emission at 355 nm and using frequency quadrupling we attained emission at 266 nm. Finally, in this work demonstrated the first picosecond diamond Raman laser pumped at 532 nm with sub-100 ps Q-switched pulses. Owing to favorable combination of pulse energy and pulse duration, we attained efficient operation of the Raman laser with emission at yellow (573 nm); the output pulses were as short as 39 ps and the output power was 143 mW, corresponding to a conversion efficiency as high as 40%. In another approach, we demonstrated Raman laser operating at 1240 nm by pumping with 1064 nm Q-switched pulses. In this case, Raman conversion resulted in optical pulses with a duration of 62 ps and 246 mW average power, which were frequency doubled to 620 nm. The corresponding pulse duration and average power at 620 nm were 46 ps and 128 mW, respectively. As third approach, under intense pumping the 620 nm was also generated directly from 532 nm, with 10 mW of average power and 24 ps pulse duration, the shortest pulses achieved in this work.

The results open a new perspective to the development of practical laser sources delivering µJ-level short optical pulses. When combined with nonlinear conversion techniques, the technology platform covers an extensive wavelength range and could find uses in a wide range of applications; for example, the 532 nm laser platform has been used successfully in time-gated Raman spectroscopy.

Preface

"*It is we who must seek the Truth of the Universe in order to achieve enlightenment.*" – Dr. Daniel Jackson

This study was carried out at the Optoelectronics Research Centre (ORC), Tampere University of Technology (TUT). I would like to express my sincere gratitude to my supervisor Prof. Mircea Guina and instructor PhD. Antti Härkönen for support and guidance in this thesis. This work was partially funded by the Academy of Finland under project number 282431 LaseREE and Tekes project number 677/31/2012 Rambus.

ORC co-authors, Ph.D. Ville-Markus Korpijärvi and M.Sc. Iiro Leino, are acknowledged. Ville-Markus for growing the state-of-the-art SESAMs used in this thesis, and Iiro, not only for electrical back-up but also for general level practical discussions.

An important part of this work was done in collaboration with Prof. Alan Kemp's group from the University of Strathclyde, Glasgow. Prof. Alan Kemp, PhD. Sean Reilly, PhD. Vasili Savitski, and Łukasz Dziechciarczyk, deserve great thanks for providing the first diamond Raman laser samples studied in this thesis, and also for valuable discussions and help regarding Raman lasers.

As this thesis concerns SESAM Q-switched microchip lasers – with the SESAM being a key component – I would like to acknowledge Jari Lyytikäinen, Soile Suomalainen and Sanna Ranta for growing the SESAMs that were also studied, but are not included in this thesis. Your contributions are acknowledged as much as other co-authors.

Most of the work is done in the lab, but many great ideas come up in the coffee breaks, pubs or other free time activities while discussing with co-workers. Thus, I would like to thank all my co-workers for the valuable discussions during the years. Special thanks are reserved for Esa Saarinen, Antti Rantamäki and Alexander (Sasha) Chamorovskiy, who I also consider as my friends.

Last but not least, I would like to thank my friends and family for the great support through the years.

As final words, I would like do express my genuine joy how the work of this thesis turned out. Though I haven't found the truth of the universe, nor am I enlightened, I have had the privilege to observe the brightness, and variety of the beautiful colors of light seeked within this thesis.

Tampere, September 2017

Jari Nikkinen

Contents

Abstract **i**

Preface **iii**

List of Abbreviations and Symbols **vii**

List of Publications **xi**

Author's Contribution **xiii**

1 Introduction **1**

2 Theory **5**
2.1 Laser cavity 5
2.2 Q-switched microchip lasers 6
2.2.1 Principles of passive Q-switching 7
2.2.2 SESAMs for passive Q-switching 12
2.3 Frequency conversion 15
2.3.1 Second harmonic generation and sum frequency generation. 15
2.3.2 Diamond Raman laser as a frequency converter 17

3 Experimental Work and Results **21**
3.1 Master-oscillators 22
3.2 Power amplification 25
3.3 Second harmonic and sum frequency generation 29
3.4 Diamond Raman lasers 32

4 Conclusion **39**
4.1 Main results and progress beyond the state-of-the art 39
4.2 Future outlook 41

Bibliography **43**

List of Abbreviations and Symbols

Abbreviations

BBO	Beta barium borate
COD	Catastrophic optical damage
Cr^{4+}	Chromium ion
DM	Dichroic mirror
Er	Erbium
FR	Faraday rotator
FLIM	Fluorescence lifetime imaging microscopy
FSR	Free spectral range
FWOT	Full-wave optical thickness
GaInNAs	Gallium indium nitride arsenate
HWP	Half-wave plate
HR	High reflectivity
Ho	Holmium
IR	Infrared
KDP	Potassium dihydrogen phosphate
LIDAR	Light detection and ranging
LiNbO3	Lithium niobate
LBO	Lithium triborate
MO	Master-oscillator
NIR	Near-infrared
Nd	Neodymium
NA	Numerical aperture
PPLN	Periodically poled Lithium niobate
PBS	Polarizing beam splitter
Pr	Prasedymium
QW	Quantum-well
QPM	Quasi-phase matching
SHG	Second harmonic generation
SESAM	Semiconductor saturable absorber mirror
STED	Stimulated emission depletion microscopy
SFG	Sum frequency generation
TEM	Transverse electromagnetic (modes)
Tm	Thulium
TGRS	Time-gated Raman spectroscopy
TPA	Two-photon absorption
TPE	Two-photon excitation

UV	Ultraviolet
VIS	Visible
Yb	Ytterbium
YAG	Yttrium aluminium garnet
YVO_4	Yttrium orthovanadate

Symbols, Greek alphabet

β	Two-photon absorption coefficient
γ	Gain reduction factor
ϵ	Function describing Q-switch
η_{OC}	Output coupling efficiency
θ	Phase-matching angle
λ	Wavelength
ν	Frequency
σ_{em}, σ_{abs}	Emission and absorbtion cross section
τ_L	Upper state lifetime
τ_p	Pulse duration
τ_{rt}	Cavity roundtrip time
τ_{SESAM}	SESAM relaxation time
ϕ	Photon density
χ	Nonlinear susceptibility
ω	(Angular) frequency

Symbols, other

A	(Mode) area
c	Speed of light
d_{eff}	Effective nonlinear coefficient
$\Delta\lambda_c$, $\Delta\nu_c$	Spectral width of a cavity mode
$\Delta\lambda_{fsr}$, $\Delta\nu_{fsr}$	Free spectral range
ΔR	Modulation depth
E	Electric field
E_{out}	Output energy
f	Focal length
F	Finesse or fluence
F_{sat}	Saturation fluence
F_2	A parameter describing the amount of two-photon absorption
g	Degeneracy or Raman gain coefficient
G	Gain
h	Planck's constant
I	Intensity
k	Wavenumber
k_{sp}, K_{sp}	Spontaneous Raman scattering factor
l	Laser gain medium length
l_{out}	Output coupling loss term
l_p	Dissipative loss term

L	Laser cavity length, or round trip dissipative loss
M	Spontaneous photon to cavity mode coupling coefficient
n	Population inversion or refractive index
n_i, n_f, n_t	Initial, final and threshold population
n_{tot}	Total density of Nd-ions
N	Normalized pump pulse duration, or number of passes
N_0	Transparency density
P	Polarization
P_P	Pump power
q_0	(Reflectivity) loss term
r	Mode radius
R_{i1}, R_{i2}	Input, output reflectivity at i:th Stokes wavelength
R_{ns}	Nonsaturable reflectivity
R_{OC}	Output coupler reflectivity
R_{SESAM}	SESAM reflectivity
R_U	Unswitched reflectivity
t	Time
W_p	Pumping rate
$\varnothing$	Diameter

List of Publications

I Nikkinen J., Korpijärvi V.-M., Leino I., Härkönen A., Guina M., "Microchip laser Q-switched with GaInNAs/GaAs SESAM emitting 204 ps pulses at 1342 nm", *Electronics Letters*, vol. 51, no. 11, pp. 850 – 852, May 2015.

II Nikkinen J., Korpijärvi V.-M., Leino I., Härkönen A., Guina M., "Frequency-doubled passively Q-switched microchip laser producing 225 ps pulses at 671 nm", *Optics Letters*, vol. 41, no. 22, pp. 5385 – 5388 Nov. 2016.

III Nikkinen J., Härkönen A., Leino I., Guina M. "Generation of sub-100 ps pulses at 532, 355, and 266 nm using a SESAM Q-switched microchip laser," *IEEE Photonics Technology Letters*, vol. 29, no. 21, pp. 1816 – 1819, Nov. 2017.

IV Nikkinen J., Savitski V., Reilly S., Dziechciarczyk Ł., Härkönen A., Kemp A. Guina M. "Picosecond monolithic diamond Raman laser emitting at 573 nm," *IEEE Photonics Technology Letters*, Submitted: Sep. 13th 2017.

Author's Contribution

This thesis includes 3 peer-reviewed journal articles and 1 manuscripts submitted for peer-reviewed journals. It also includes some supplementary unpublished data. The author's contribution to these publications is described below.

I The author has processed the microchip laser used in this work, he has designed and prepared the experimental setup, carried out all measurements and analyzed the data. The author has designed and fabricated the custom coating used between the SESAM and the gain crystal. The author has written most of the paper. The SESAM was fabricated by V.-M. Korpijärvi, and designed as group work. The custom electronics used in the work were designed and fabricated by I. Leino.

II The author has processed the microchip laser used in this work, he has designed and prepared the experimental setup, including the amplifier, carried out all measurements and analyzed the data. The author has designed and fabricated the custom coating used between the SESAM and the gain crystal. The author has written most of the paper. The SESAM was fabricated by V.-M. Korpijärvi, and designed as group work. The custom electronics used in the work were designed and fabricated by I. Leino.

III The author has processed the microchip laser used in this work, he has designed and prepared the experimental setup, carried out all measurements and analyzed the data. The author has written most of the paper. The SESAM used in this work was provided by RefleKron Oy. The custom electronics used in the work were designed and fabricated by I. Leino.

IV The author has processed the microchip laser used in this work, he has designed and prepared the experimental setup, carried out all measurements and analyzed most of the data. The author has written a significant part of the paper. This work has been carried out in collaboration with Prof. A. Kemp's group from the University of Strathclyde, Glasgow, who kindly provided the Raman crystal. The Strathclyde team has designed the coating reflectivities, provided technical instructions, and helped in analyzing the results. Mathematical modeling of the results was done by Ł. Dziechciarczyk and V. Savitski. The manuscript has been written jointly by the Tampere and Strathclyde teams.

1 Introduction

Lasers – light amplification by stimulated emission of radiation – are devices producing monochromatic coherent light with high brightness [1]. Since the introduction of the first laser in 1960 by Maiman [2], these light sources have made their way out from the research laboratories and have become an important part of the modern society. Lasers enable, for example, high-speed optical telecommunication, advanced manufacturing and manipulation of materials and a growing range of other applications in science, metrology, industry, medicine and defense. We commonly utilize the capability of light to transmit information (e.g. in telecom [3] and sensing [4]) and energy (e.g. optical pumping [5], laser cutting and welding [6]), and interact with matter in a particular way (e.g. to enable nonlinear optics [7], Raman spectroscopy [8], or athermal laser cutting). Moreover, light has been always essential to the advance of fundamental knowledge, and is currently used to define the unit of time and measure distance at accuracy never seen before (e.g. detection of gravitational waves via laser interferometry [9, 10]). The potential of optical technologies has always existed, but only the introduction of the laser made it practically possible to use photons for so many things.

Different types of lasers are often classified by their gain material from gas lasers to dye, fiber, solid-state and semiconductor lasers, all having their unique properties, such as operation wavelength, power, brightness, efficiency and tunability [1]. Lasers are also commonly categorized by their operation mode into continuous wave lasers and pulsed lasers. A laser can be pulsed simply by turning on and off a continuous wave laser. More sophisticated pulsing technologies, such as gain switching [11, 12], cavity dumping [13, 14] and Q-switching [15–17], aim at storing and accumulating energy in the system for a long period of time, and then releasing it very rapidly. Thus, these lasers can momentarily produce intensities that are several orders of magnitude higher than available from a similar continuous wave laser [18]. The shortest optical pulses are generated with a technique called mode-locking [19–21], where several laser modes are "locked" together, forming a pulse that circulates back and forth within the laser oscillator [18].

By using a pulsed master-oscillator and power amplification, it is reasonably easy to generate 100 kW peak power [22, 23], sub-ns pulses, in a beam that can be focused to a $\sim$10 µm diameter spot. Thus, we can produce optical intensities of the order of several GW/cm^2 addressing specific application needs. For a point of comparison, it is good to notice that a typical nuclear power plant produces about 1 GW of power [24]. The motivation for generating short optical pulse often arises from this particular capability to reach extreme intensities, which allow various nonlinear optical effects to take place. Short pulses also enable us to study and observe physical and chemical phenomena in a very short time scale. One additional advantage of pulsed lasers is the small thermal load (with respect to the peak power) that they may pose on a target sample at hand.

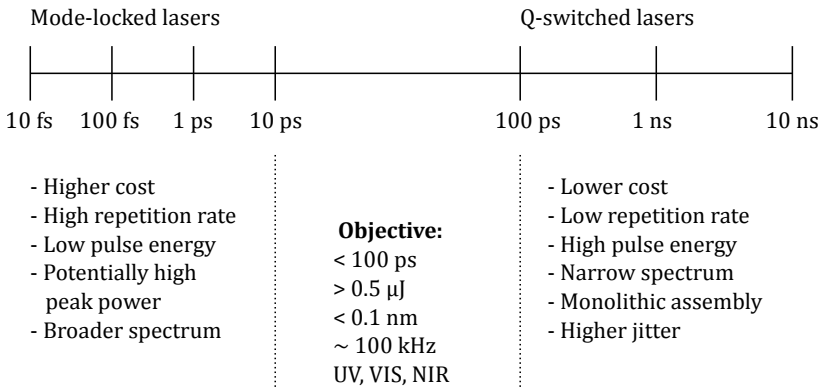

Figure 1.1: Comparison of mode-locked and Q-switched lasers divided into their typical operating regimes. Objective of this thesis is to narrow the gap between these two technologies.

All technologies used to obtain short optical pulses have their advantages and disadvantages. For example, most mode-locked lasers operate with a pulse duration in the range of a few fs - 30 ps and repetition rate of 20 MHz - hundreds of GHz, mode-locked pulses do not carry much energy, and if they do, that usually requires high average output powers that complicate system designs and increase the cost significantly. On the other hand, Q-switched lasers operate with much lower repetition rates varying typically in the range of a few Hz – few MHz, and pulse duration of sub-nanosecond to tens of nanosecond. [5]. Due to low repetition rate and longer pulse duration, a Q-switched lasers typically produce pulses with much higher energy than a mode-locked laser having the same average output power. On the other hand, Q-switched laser can mainly attain the ns pulse regime, leaving ps range fully dominated by mode-locked lasers. These differences in the output properties have divided mode-locked lasers and Q-switched lasers into very different application areas: mode-locked lasers cover less cost-sensitive, high-end applications with requirement for sub-30 ps pulses, whereas nanosecond Q-switched lasers are often used for tasks requiring lower repetition rate or high pulse energy. In terms of pulse duration, the coverage of mode-locked and Q-switched lasers do not overlap. There actually exists a gap where neither lasers are very good. For simplicity, we can call this gap the 10 – 100 ps pulse regime. If we look at the repetition rate or pulse energy, the gap becomes even wider and more difficult to fill. There are simply not many options available today for a low repetition rate (1 Hz – 1 MHz) laser with 10 – 100 ps pulse duration and reasonably high pulse energy (>1 µJ). Even less so, if the wavelength or spectral width are specified tightly. If cost is not an issue, all requirements can be probably met with a mode-locked laser, followed by a pulse picker [25, 26] and multiple stages of power amplification, or a regenerative amplifier [27, 28]. The cost of such a system is, however, often prohibitive.

From this stand point, **the goal for this work was to narrow the gap between mode-locked lasers and traditional nanosecond Q-switched lasers**. This task was **motivated by the need to offer practical technological solution for applications** where lower cost short pulse laser could make a difference, such as time-gated Raman spectroscopy (TGRS) [29, 30], two-photon polymerization [31, 32] (additive manufacturing), fluorescence lifetime imaging microscopy (FLIM) [33], stimulated emission depletion microscopy (STED) [34], and two-photon excitation (TPE) [35].

This particular work was initiated in 2014, with a target to develop a robust, low-cost, low-repetition rate, narrow bandwidth, sub-100 ps green (532 nm) laser for time-gated Raman spectroscopy. The work has later expanded to cover also other wavelengths (UV, yellow, red and NIR) and in consequence advance the understanding of new laser physics, develop broader technology base, and potentially address more applications.

One part of the work has concentrated on the development of Q-switched microchip lasers and generation of short infrared pulses. Another part has covered amplification of the pulsed signal to levels enabling efficient nonlinear conversion. The third part deals with expanding the wavelength coverage. In terms of broad technical targets, the **aim of this thesis was to extend the sub-100 ps Q-switched microchip lasers to wavelength range from UV, to visible and near-infrared**. From an application perspective, the aim was to develop laser sources that are compact, robust, reliable, low-cost, and have the following parameters:

- Pulse duration: <100 ps
- Repetition rate: 100 kHz (from pulse on demand to MHz)
- Pulse energy: >0.5 µJ (power >50 mW at 100 kHz)
- Power: >50 mW
- Wavelength: UV, VIS, NIR
- Spectral width: <0.1 nm

In the following chapters of the thesis, I will summarize the design and theoretical considerations of the Q-switched microchip laser, describe the experimental work and results, and finally draw conclusions on the work and future perspective. The structure in each section follows the modular architecture of the system, starting from the master-oscillator, followed by the power-amplifier and ending with two methods of frequency conversion: harmonic generation and conversion in a Raman laser.

2 Theory

All lasers are comprised of three main components: gain, feedback and pump [18]. The gain provides optical amplification, the feedback enables stimulated emission, and the pump provides the energy to the system. In this chapter, I will briefly describe the main theoretical aspects essential in behavior of the laser system used in this thesis, starting from general description of Fabry–Pérot cavity, continuing to general concept to switch the cavity, and then describing operation of Q-switched microchip lasers. Moreover, the basic concepts underpinning the frequency conversion methods employed to reach visible and UV wavelengths are discussed.

2.1 Laser cavity

To sustain stimulated emission and obtain lasing the gain material is placed in a feedback system, typically consisting of mirrors forming a Fabry–Pérot cavity, such as the one shown in Figure 2.1. The design of the cavity affects several important properties of the laser including spectral properties (longitudinal modes), the beam quality (transversal modes), and stability of the laser cavity.

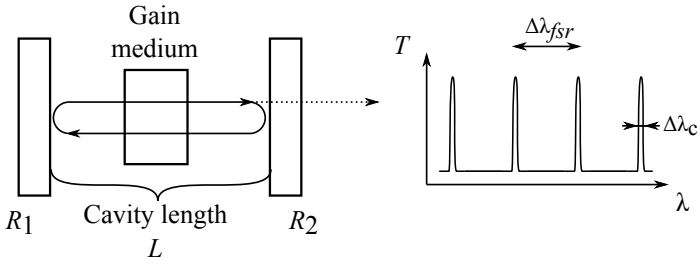

Figure 2.1: A schematic presentation of a laser cavity and cavity mode spacing.

The Fabry–Pérot cavity supports only a discrete number of resonant cavity modes, which in a laser are also called longitudinal modes [1]. The frequency spacing of the Fabry–Pérot cavity modes is inversely proportional to the optical length of the cavity and is given by [1]

$$\Delta\nu_{fsr} = \frac{c}{2L_{opt}} = \frac{c}{2nL}, \tag{2.1}$$

where c is speed of light and $L_{opt} = nL$ is optical cavity length, n is refractive index and L is physical length of the cavity [1]. The mode spacing $\Delta\nu_{fsr}$ is also known as free spectral range (FSR).

The spectral width $\Delta\nu_c$ of the cavity modes is defined by the free spectral range and the finesse, F, of the cavity, [1]

$$\Delta\nu_c = \frac{\Delta\nu_{fsr}}{F}. \tag{2.2}$$

The cavity finesse can be defined by

$$F = \frac{\pi(R_1R_2)^{(1/4)}}{1-(R_1R_2)^{(1/2)}}, \tag{2.3}$$

where R_1 and R_2 are the mirror reflectivities and the cavity is assumed lossless [1].

Most lasers operate with several longitudinal modes, however in this work, the cavity lengths are sufficiently short to support only one longitudinal mode within the gain bandwidth, leading to single-frequency laser operation.

The field distribution in the Fabry–Pérot resonator must reproduce itself after each round trip [36]. Such field distributions are called transversal cavity modes. A laser cavity can contain several transversal modes, in which case it is called a multimode laser. In most cases, single transversal mode operation is preferred due to better beam quality. Multimode transversal operation can also result in multiple longitudinal mode operation and therefore increased spectral width. Single transversal mode operation is usually forced by designing the resonator in such a way that the fundamental Gaussian TEM_{00}-mode closely overlaps with the pumped gain area leaving no gain for higher order transversal modes. In this work, we have aimed for single-frequency operation. For this reason, the laser must be operated also with single transversal mode. Thus the pump spot sizes in thesis are closely matched to the TEM_{00}-mode of a cavity. [1, 37]

Stability of the cavity means that a ray injected into the optical system will repeat its path (direction and position) even after multiple round trips in the cavity [36]. In case of unstable cavity the optical power will diverge indefinitely away from the cavity axis [1]. The stability of the cavity is determined by its geometry, i.e. the curvature of the mirrors and the distance(s) between the mirrors. The cavity geometry and stability is easy to simulate using ABCD ray tracing matrix formalism. [1] In this work we have used a plane-plane laser cavity, stabilized by a thermal lens, caused by the heating in the pumped area. [18, 36]

2.2 Q-switched microchip lasers

Soon after the first demonstration of a laser in 1960 by T. H. Maiman [2] Hellwarth and McClung demonstrated that very high intensity pulses can be created by switching the cavity Q-value [38, 39]. In 1963 Wagner and Lengyel derived the first mathematical model and approximated solution for the *"evolution of the giant pulse in a laser"* and for its pulse energy, peak power and pulse duration [40]. Then Erikson *et al.* [41, 42] extended the work to passive Q-switching. Quite much later from this seminal work, Spühler *et al.* [43] extended the equations for passively Q-switched microchip lasers based on semiconductor saturable absorber mirrors (SESAMs), while Butler *et al.* in 2012 [44] derived a rate equation model including a part describing effective photon fluence and evolution of a SESAM reflectivity. From this historical development perspective, in this chapter we review the key concepts underpinning the operation of Q-switch microchip-lasers.

2.2.1 Principles of passive Q-switching

Cavity quality factor, Q, is defined as the ratio of the energy stored in the cavity to the energy loss per cycle [1]

$$Q = 2\pi \times \frac{\text{energy stored}}{\text{energy loss per cycle}} = 2\pi \frac{2L\nu}{c\alpha_{loss}}. \tag{2.4}$$

Then Q-switching is a technique used to generate high energetic pulses by altering the cavity Q-factor between a low value and a high value. Thus, the cavity Q is initially kept low, i.e. high losses, to prevent the lasing action. In this case, under constant pumping the energy is stored into the gain material and the population inversion reaches a level far above the threshold for normal lasing action. When cavity Q factor is then switched to high Q, low losses, the stored energy in the gain material is suddenly released in the form of a short energetic optical pulse [1, 5]. A schematic of a Q-switched laser and principle time evolution is shown in Figure 2.2.

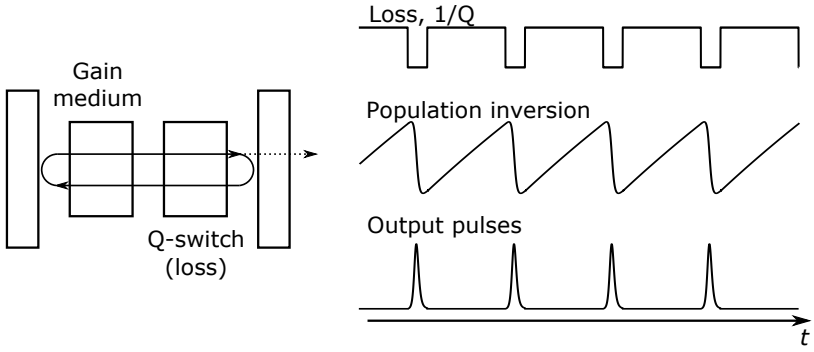

Figure 2.2: A schematic presentation of a Q-switched laser setup on the left with loss, population inversion and output evolution on the right.

Q-switched lasers are divided by the way the cavity Q is switched into two main classes: active and passive Q-switching, respectively. Active Q-switching is achieved with an external modulator, while passive Q-switching is achieved using a saturable absorber initiating a self-switching mechanism. [36]. Q-switches are further divided into slow and fast Q-switches, where fast Q-switches are those where Q-value is changed so fast that within the switching time the population inversion has not changed considerably. In a case of ideal Q-switch, the function ($\zeta(t)$) describing the change of cavity Q can be considered as a step-function, and for such ideal case one can derive analytical approximations for the output energy [5, 40].

In general, the evolution of the population inversion n and the photon density ϕ over time t, for a Q-switched laser, can be described as generalized rate-equations [5, 37]

$$\frac{\mathrm{d}n}{\mathrm{d}t} = -c\gamma\sigma_{\mathrm{em}} n\phi + W_p \tag{2.5}$$

$$\frac{\mathrm{d}\phi}{\mathrm{d}t} = \left(c\sigma_{\mathrm{em}} n \frac{l}{L} - \frac{\epsilon(t)}{\tau_{\mathrm{rt}}} \right) \phi, \tag{2.6}$$

where $\epsilon(t)$ represents the time dependent equation for the losses including the Q-switch. The other constants are speed of light c within the medium, "inversion reduction factor"

γ, emission-cross section σ_{em}, pumping rate W_p, gain length l, cavity length L, and cavity round trip time τ_{rt}. The loss function can be represented as $\epsilon(t) = -\ln R_{\mathrm{OC}} + \delta + \zeta(t)$, where R_{OC} is the output coupler reflectance, δ stands for additional cavity losses and $\zeta(t)$ represents the Q-switch.

As a solution [5, 40] to the generalized rate equations the output energy of the Q- switched laser can be expressed as

$$E_{\mathrm{out}} = \frac{h\nu A}{2\sigma_{\mathrm{em}}\gamma} \ln \frac{1}{R_{\mathrm{OC}}} \ln \frac{n_i}{n_f}, \tag{2.7}$$

and pulse duration as

$$\tau_p = \tau_{rt} \frac{n_i - n_f}{n_i - n_t[1 + \ln(n_i/n_t)]}, \tag{2.8}$$

where $h\nu$ is the output photon energy, A is the mode area, R_{OC} is the output coupler reflectance, and the n_x are the initial n_i, final n_f, and threshold n_t populations. Thus, the pulse energy and the pulse duration are dependent on amount of population inversion and the change in population $(n_i - n_f)$, which are highly depended on the type of the Q-switched laser. As it can be seen in equation (2.8) the pulse duration depends on cavity round trip time, and, as a consequence, on the cavity length. Therefore, the shortest pulse duration (16 ps [45]) has been obtained in a so called microchip laser.

Microchip lasers, first introduced by Zayhowski *et al.* [46], are a type of laser where a thin chip of solid-state gain material forms the resonator. Such microchips can be passively Q-switched by introducing a saturable absorber into the cavity. [47]. A schematic presentation of such passively Q-switched microchip laser is shown in Figure 2.3.

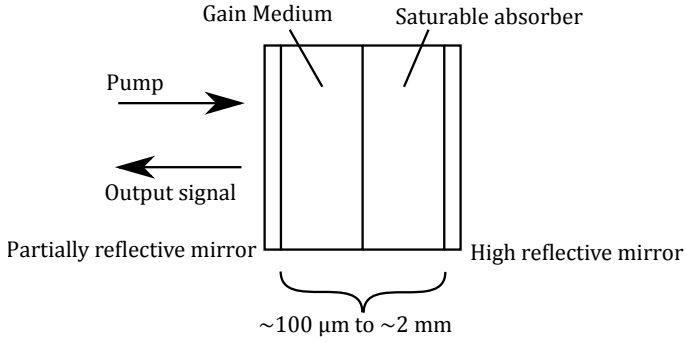

Figure 2.3: A schematic presentation of a passively Q-switched microchip laser.

Q-switched microchip lasers allow the generation of short pulses with durations typically below 1 ns [36]. The passive Q-switching also offers the advantage of an exceptionally simple and small design, which leads to robust, and low-cost systems [5, 46].

Nowadays, the most common saturable absorber material for Q-switch is Cr^{4+}:YAG [5, 36], which has been used to generate pulses with durations down to 237 ps [48], corresponding to a total cavity length of 2.7 mm. As short as they may seem, for such saturable absorber the gain length l is significantly shorter than the cavity length L, reducing the net gain by factor l/L in equation (2.6) and increasing the pulse duration. One way to

keep the cavity length close to the length of the gain element is to use co-doped self Q-switching materials [49], i.e. in this case the gain and absorber section are in the same host material ($l = L$). Nevertheless, the thickness of the solid-state saturable absorbers (>100 µm) cannot be made as thin as that of semiconductor saturable absorbing mirrors (SESAMs) as those we employed in this work. Typically a semiconductor mirror structure incorporating a saturable absorber which is only a few microns (<10 µm) thick [50]. The main difference in terms of thickness requirements for semiconductor and solid-state absorbers is given by the absorption cross-section and density of atoms, which are much higher in semiconductors. In addition, semiconductors allow tailoring of the amount of absorption as discussed in more detail in section 2.2.2.

Using the rate equation model by Butler *et al.* [44] the behavior of a SESAM Q-switched microchip laser can be expressed by the following coupled rate equations

$$\frac{\mathrm{d}n}{\mathrm{d}t} = -c\sigma_{\mathrm{em}} n\phi + \frac{P_P}{h\nu_P}\frac{1}{\pi r^2 l_{\mathrm{L}}}(1-\exp[-2(n_{\mathrm{tot}}-n)\sigma_{\mathrm{abs}} l_L]) - \frac{n}{\tau_{\mathrm{L}}} \tag{2.9}$$

$$\frac{\mathrm{d}\phi}{\mathrm{d}t} = c\sigma_{\mathrm{em}} n\phi - \frac{-\ln[R_{\mathrm{OC}} R_{\mathrm{SESAM}}(F)]}{\tau_{\mathrm{rt}}}\phi + M\frac{n}{\tau_{\mathrm{L}}} \tag{2.10}$$

$$\frac{\mathrm{d}F}{\mathrm{d}t} = ch\nu_{\mathrm{L}}\frac{\phi}{2} - \frac{F}{\tau_{\mathrm{SESAM}}}, \tag{2.11}$$

where the SESAM reflectance is given by [44]

$$R_{\mathrm{SESAM}}(F) = R_{\mathrm{U}} + \Delta R(1-\exp(-F/F_{\mathrm{sat}})) \tag{2.12}$$

or by more commonly used equation [51, 52]

$$R_{\mathrm{SESAM}}(F) = \frac{R_{\mathrm{ns}} F_{\mathrm{sat}}}{F}\ln\left(1+\left[1-\frac{\Delta R}{R_{\mathrm{ns}}}\right]\left[\exp\left(\frac{F}{F_{\mathrm{sat}}}\right)-1\right]\right), \tag{2.13}$$

where R_u is unswitched reflectance, 1-R_{ns} is nonsaturable losses, ΔR is modulation depth, F and F_{sat} are fluence and saturation fluence. These parameters are illustrated in Figure 2.4. Other constants in the rate-equations are pump power P_P, mode radius r, cavity and gain length $l = L$, total density of Nd-ions n_{tot}, photon to cavity mode coupling efficiency M, upper state lifetime τ_L, frequencies of laser ν_L and pump ν_P light, and relaxation time of the SESAM τ_{SESAM}.

In order to solve accurate output characteristics of a Q-switched microchip laser one must solve the rate equations numerically. An example of the numeric evolution the rate equations (2.6), using own code implemented in Matlab, is shown in Figure 2.5b showing the evolution of the population inversion, cavity photon density and effective photon fluence evolution over time.

In the case of small modulation depth, however, Spühler *et al.* [43] introduced approximate solutions to the rate equations as follows. For the pulse duration

$$\tau_p \approx \frac{3.52\tau_{\mathrm{rt}}}{q_0} \approx \frac{3.52\tau_{\mathrm{rt}}}{\Delta R} = \frac{3.52L}{c_n \Delta R}, \quad (\text{when} \quad \Delta R \approx q_0) \tag{2.14}$$

where q_0 is defined by equation $\Delta R = 1 - \exp(-q_0)$. Moreover, the pulse energies can be approximated as

$$E_p = \frac{h\nu_L}{2\sigma_{\mathrm{em}}} A 2\Delta R \eta_{\mathrm{OC}}, \quad (\text{when} \quad \Delta R \approx q_0) \tag{2.15}$$

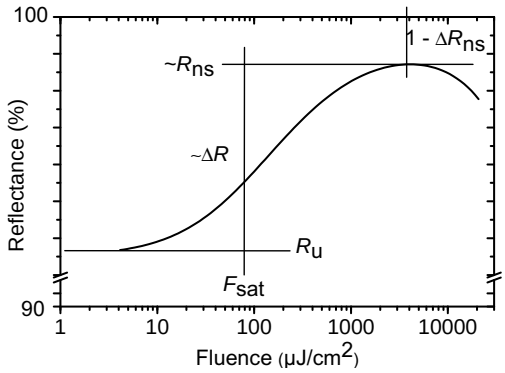

Figure 2.4: Nonlinear reflectance curve of a SESAM showing the reflectance change as a function of fluence.

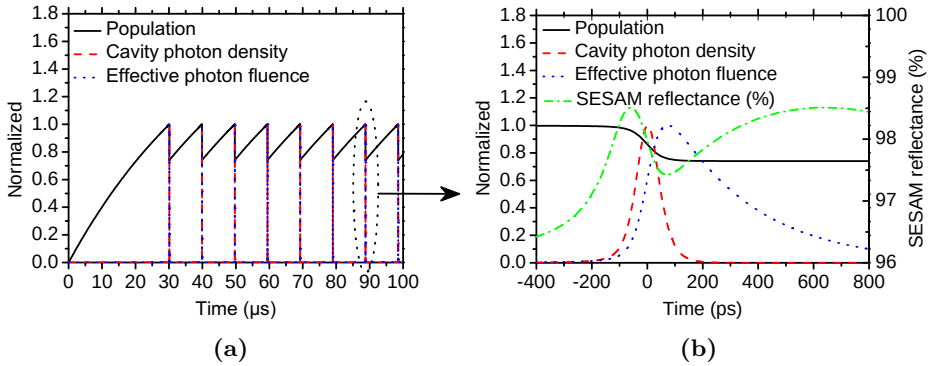

Figure 2.5: Normalized numerically solved rate equations for a SESAM Q-switched microchip with typical parameters of $\sigma_{em} = 2.5 \cdot 10^{-22}$ m^2, $n_{tot} = 3.75 \cdot 10^{26}$ m^{-3}, $\sigma_{abs} = 5.46 \cdot 10^{-24}$ m^2 (c-axis of Nd:YVO_4), $L = 100$ µm, $R_{OC} = 90$ %, $R_{ns} = 99$ %, $\Delta R = 3$ %, $F_{sat} = 100$ µJ/cm^{-2}, $\tau_{\mathrm{SESAM}} = 300$ ps, $F_2 = 500 \cdot 10^3$ µJ/cm^{-2}. Output result is 98 ps pulse duration and 102 kHz repetition rate. (a) 100 µs long pulse train starting from initial condition $n(0) = \phi(0) = F(0) = 0$ and (b) detail during a single pulse.

where output coupling efficiency $\eta_{\mathrm{OC}} = l_{\mathrm{out}}/(l_{\mathrm{out}} + l_p)$, and losses are further defined as $T_{\mathrm{out}} = 1 - R_{\mathrm{OC}} = 1 - \exp(-l_{\mathrm{out}})$ for output coupling while l_p counts for other nonsaturable losses. Furthermore, the peak power can be calculated from the pulse energy and the pulse duration as

$$P_{\mathrm{peak}} \propto \frac{E_p}{\tau_p} \propto \frac{(\Delta R)^2 A}{\tau_{\mathrm{rt}} \sigma_{\mathrm{em}}} \eta_{\mathrm{OC}}, \qquad (\text{when} \quad \Delta R \approx q_0). \tag{2.16}$$

Previous equations also assumes that $(l \geq q_0)$ [43].

From equation (2.14), it be can seen that the shorter the cavity and larger the modulation depth, the shorter the pulse duration becomes. However, for a given gain material there is a limit were the material gain "(σ_{em})" has to exceed the losses of a saturable absorber. Equations (2.15) and (2.16), on the other hand reveal that pulse energy and peak power are reduced with high σ_{em} materials. Within this thesis, short pulses are the main objective rather than high pulse energies and thus high emission cross section materials

are favored.

Neodymium doped crystals Nd^{3+}:YVO_4 and Nd^{3+}:YAG have the highest emission cross sections of all solid-state gain materials, and they are the most commonly used gain materials for microchips [5]. Nd:YVO_4 has higher emission and absorption cross section than the YAG and thus it is more commonly used in microchips and preamplifiers, where as Nd:YAG is used in high power amplifiers for its much higher thermal conductivity and saturation fluence. Energy-level diagram of a Nd:YVO_4 is presented in Figure 2.6, showing two major emission lines at 1064 nm and 1342 nm.

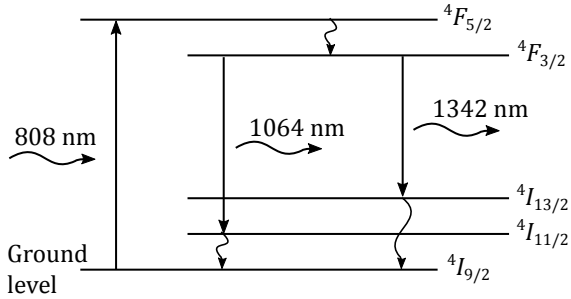

Figure 2.6: Energy-level diagram of neodymium doped YVO_4 showing two major emission lines at 1064 nm and 1342 nm. The emission cross sections vary in the range of about $25 \cdot 10^{-23}$ m^2 [44] to $12 \cdot 10^{-23}$ m^2 [53] at 1064 nm and $6 \cdot 10^{-23}$ m^2 [53] at 1342 nm

Thermal management is also an important concern for lasers. The most important effect of the heat load in SESAM Q-switched microchip lasers is a change in emission cross section of the gain medium [54]. For 0.1% neodymium doped YVO_4 gain material the emission cross section is reduced by about 44% [55] between temperatures of 16 °C and 80 °C, with gain peak shift of about 3 pm/°C [55] to 4.7 pm/°C [56]. Thermal expansion coefficients are $1.76{\cdot}10^{-6}$/°C and $8.24{\cdot}10^{-6}$/°C while change in refractive indexes ($\mathrm{d}n/\mathrm{d}T$) are $15.5{\cdot}10^{-6}$/°C and $8.41{\cdot}10^{-6}/°C$ for c-axis and a-axis directions, respectively [57]. Furthermore, thermal conductivity of YVO_4 is 5.5 W/m·K and 6.5 W/m·K for a- and c-axis respectively [58]. Considering that typical thermal conductivity of a semiconductor is about 5 times larger (55 W/m·K for GaAs [59]), the gain medium suffers mostly from heat, and it will be seen in [P1] that simply, by mounting the microchip to a metal block will give sufficient amount of cooling, without any further cooling of the metal block. As for the pulsing mechanism on the other hand, the temperature dependent emission cross section is crucial parameter. The heating does not introduce extra losses in the cavity but lowers the laser gain, leading to higher pulse energies [54]. Finally, it should be noted that the thermal management becomes very crucial in amplifiers where the pump power are several Watts, whereas microchips in this thesis operates only at a few hundreds of mW.

2.2.2 SESAMs for passive Q-switching

Semiconductor saturable absorber mirros (SESAMs) contain a semiconductor Bragg mirror and an absorber section, which for Q-switching can typically made of bulk or quantum-well (QW) material. The key advantages of SESAMs are that one can rather freely tailor the key parameters such as recovery time, operation wavelength, modulation depth, and saturation fluence, while the use is also simple [50].

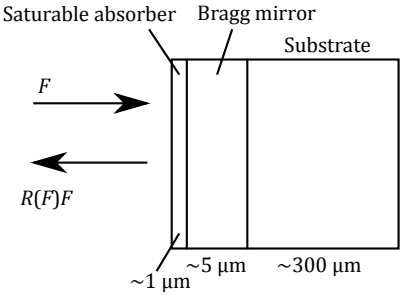

Figure 2.7: A schematic presentation of a SESAM.

The Fresnel reflection at the semiconductor – air interface and the Bragg reflector create a microcavity, which may be resonant or anti-resonant in respect with the laser wavelength [36]. For fully resonant structure, the microcavity is $n\lambda/2$ thick, while for anti-resonant operation the thickness of the microcavity is $n\lambda/2 + \lambda/4$ thick, where n is number of half-waves. Figure 2.8 reveals design and reflectivity characteristics for typical resonant and antiresonant SESAMs, employing multiple QWs. In this case, the absorber employs two groups of 3 QWs placed at 2 antinodes of the standing optical field within the microcavity. Antiresonant designs have a lower field enhancement in the absorber and thus a lower modulation depth in addition to a higher saturation fluence and higher damage threshold.

As seen in the Q-switching theory the most important parameters are the modulation depth ΔR and saturation fluence F_{sat}. The other important parameters are the nonsaturable reflectance R_{ns} (leading to insertion losses during laser operation), and two photon absorption (F_2) effect (leading to heat and degradation of the structure). The modulation depth is the maximum nonlinear change in reflectance, which can be tuned mainly by number of quantum wells, or the thickness of the bulk absorber. In addition, the degree of optical field enhancement in the absorber structure is very important factor for both modulation depth and saturation fluence. This effect can be clearly seen in Figure 2.8 between the two boundary cases of resonant and antiresonant. For any given absorber, if the field enhancement or resonance is changed, the product of modulation depth and saturation fluence remains constant [52]:

$$\Delta R F_{\mathrm{sat}} \approx N_0 h\nu = \text{constant}, \tag{2.17}$$

where N_0 is transparency density and $h\nu$ is the photon energy. Between these two parameters, the saturation fluence has little effect on the pulse formation in Q-switching, where as the modulation depth is the single most important parameter defining the pulse duration. Thus, modifying the resonance gives freedom to tailor the pulse duration.

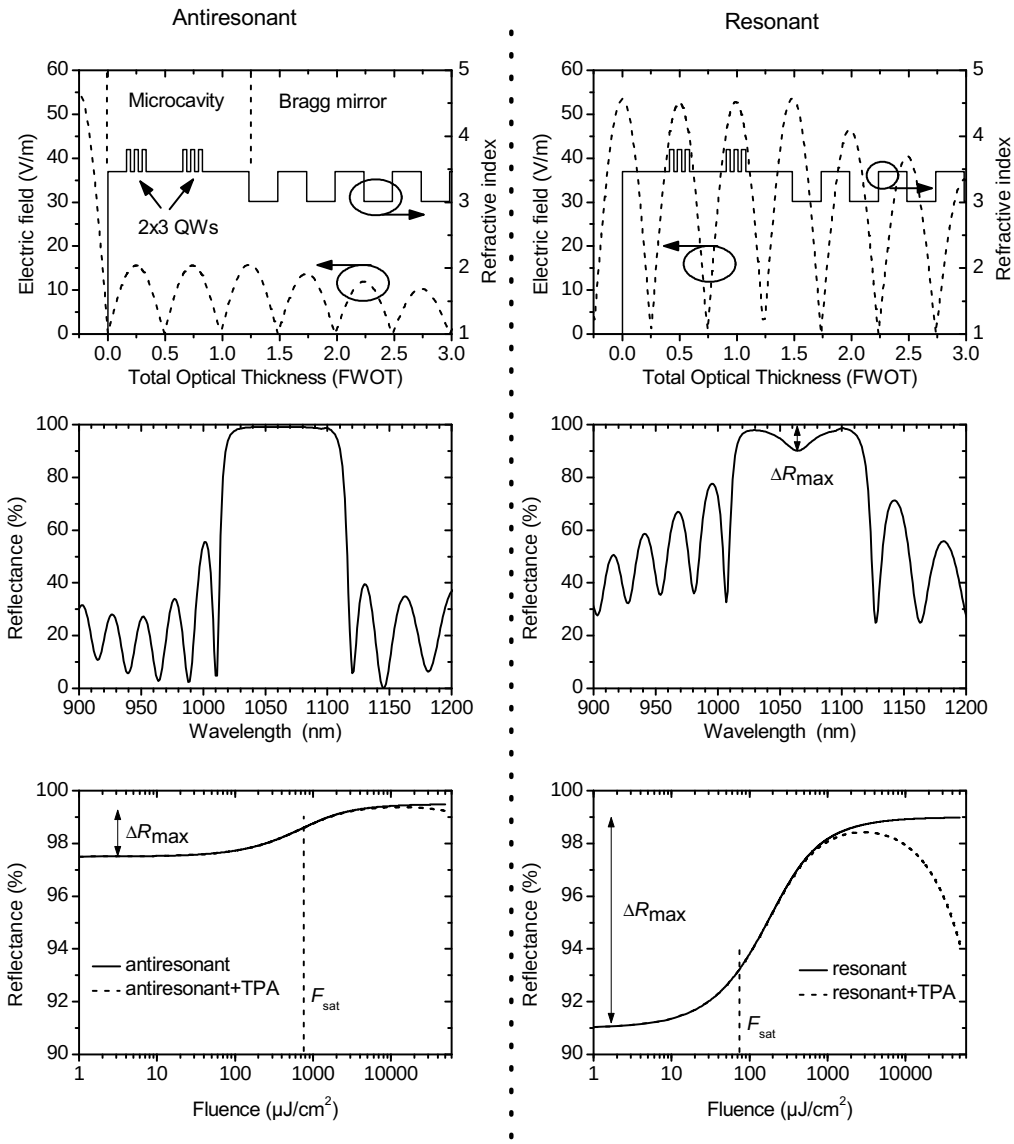

Figure 2.8: Comparison of antiresonant (left) and resonant (right) SESAM design. (top) refractive index structure of the SESAMs and the electric field distribution in the SESAM, (middle) low intensity reflectance curves, and bottom, nonlinear reflectance curves. QW: quantum-well, FWOT: full wave optical thickness, TPA: two-photon absorption.

The nonsaturable losses are always unwanted, only reducing pulse energy and typically leading only to device heating. However, with Q-switched low repetition rate lasers the effect is not as crucial, as for mode-locked lasers. The nonsaturable losses are mainly caused by linear absorption of semiconductor materials of the SESAM, too fast recovery times, and non-ideal reflectance of the Bragg mirror. For Q-switching the recovery time should be longer than the pulse duration, so that the SESAM absorption does not recover during the pulse, and increase losses.

For short and intense pulses of Q-switched lasers the two-photon absorption may become far greater loss term than the nonsaturable losses. The two-photon absorption is intensity dependent and can be written as [44]

$$I = \frac{I_0}{1 - \beta I_0}, \tag{2.18}$$

where β is the two-photon absorption coefficient. In SESAM reflectance function the two-photon absorption can be taken into account also by multiplying the reflectance function (2.13) by [51]

$$\times \exp(-\frac{F}{F_2}), \tag{2.19}$$

where F_2 is a parameter describing the amount of two-photon absorption [50, 60]. Since, the two-photon absorption is intensity depended, a resonant design with higher enhancement of the electric field leads to higher two-photon absorption, at high fluence. Too high two-photon absorption can lead to catastrophic optical damage (COD) of the SESAM [52]. From this point of view anti-resonant SESAMs are desired over resonant design. As for the pulse formation and pulse duration [44], the two-photon absorption has little effect, but on the other hand, it will reduce pulse-energy and increase repetition rate.

2.3 Frequency conversion

In general, the operation wavelengths of lasers is strictly related to the properties of the gain material, often not covering the needs of important applications. To this end, nonlinear conversion has emerged as a flexible approach in expanding the wavelength range, in particular when high peak power is available. The most used nonlinear conversion techniques are harmonic generations, Raman shifting, four-wave mixing, sometimes all of them acting simultaneously as in the case of supercontinuum laser. In this thesis, two different methods of frequency conversions are used; harmonic frequency conversion and Stokes shift in a Raman laser, which are used separately or combined in cascaded processes.

2.3.1 Second harmonic generation and sum frequency generation.

Second harmonic generation and sum frequency generation are the two most commonly used frequency conversion methods. A schematic presentation of energy diagram corresponding to these is shown in Figure 2.9. More generally, the nonlinear optical conversions are described by nonlinear optical polarization.

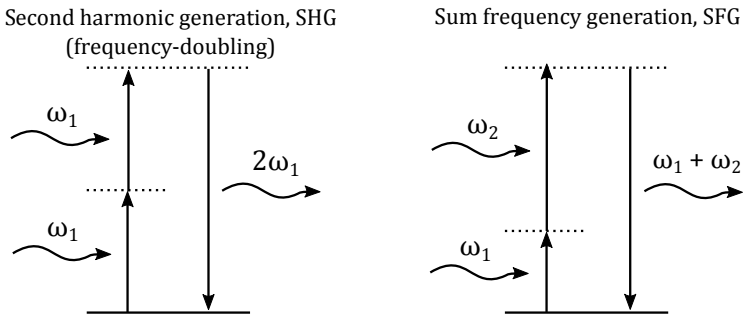

Figure 2.9: Schematic of second harmonic generation and sum frequency generation.

Under intense electric field the polarization of a medium can be written as [61]

$$\widetilde{\boldsymbol{P}}(\boldsymbol{r},t) = \epsilon_0[\boldsymbol{\chi}^{(1)}\widetilde{\boldsymbol{E}}(t) + \boldsymbol{\chi}^{(2)}\widetilde{\boldsymbol{E}}^2(t) + \boldsymbol{\chi}^{(3)}\widetilde{\boldsymbol{E}}^3(t) + \ldots], \tag{2.20}$$

where $\boldsymbol{\chi}^{(n)}$ is the n:th order susceptibility and $\boldsymbol{E}$ is the electric field of a input light. The second order susceptibility $\chi^{(2)}$ is responsible for the second harmonic and sum frequency generation, and the second order polarization in a Cartesian coordinate system can be written as [5]

$$P_j = \epsilon\chi^{(2)}_{ijk}E_jE_k, \tag{2.21}$$

where $\chi^{(2)}_{ijk}$ is a third rank tensor of 27 independent coefficient. However, under Kleinman symmetry and using contracted notation ($d_{ijk} = 1/2\ \chi_{ijk}$) the second order susceptibility can be presented as 3×6 matrix d_{il}. The nonlinear polarization can then be presented for second harmonic generation as

$$P(2\omega) = 2d_{eff}E(\omega)^2, \tag{2.22}$$

and for sum frequency generation as

$$P(\omega_1 + \omega_2) = 4d_{eff}E(\omega_1)E(\omega_2), \tag{2.23}$$

where d_{eff} is the material dependent effective nonlinear coefficient for a given input polarization and the electric fields $E(\omega_n)$ at frequency ω_n [61]

In terms of intensity, as $I = E^2$, the output intensity is related to the input intensity as

$$I(2\omega) \propto d_{eff}^2 I(\omega)^2 \tag{2.24}$$

and

$$I(\omega_1 + \omega_2) \propto d_{eff}^2 I(\omega_1)I(\omega_2). \tag{2.25}$$

The effective susceptibility (or the effective nonlinear coefficient d_{eff}) is dependent on crystal class and input field conditions. For a negative uniaxial crystal of crystal class 3m the effective susceptibility can be calculated as

$$d_{\text{eff}} = d_{31} \sin - d_{22} \cos\theta \sin 3\phi, \tag{2.26}$$

for type I condition, where the two (input) lower-frequencies have the same polarization and

$$d_{\text{eff}} = d_{22} \cos^2\theta \sin 3\phi, \tag{2.27}$$

for type II, where the polarizations are orthogonal. The θ angle is the angle between the propagation direction and the crystalline z-axis and ϕ is the azimuthal angle between the propagation direction and the xz crystalline plane [61].

Efficient harmonic generation also requires phase-matching ($\Delta k = 0$), where the sum of wave numbers equals 0 ($n_1\omega_1 + n_2\omega_2 = n_3\omega_3$). This means that interacting fundamental and frequency converted light are in the same phase, and the phase-matching is maintained along the propagation direction. Due to chromatic dispersion ($n(\omega_1 + \omega_2) > n(\omega_2) > n(\omega_1)$), phase-matching conditions are achieved only in birefringent crystals, where the same refractive index is found along different crystalline axes for different wavelengths. In other words by polarizing the interacting fields along different crystalline axes. Furthermore, angle phase-matching, also called critical phase-matching can be ensured by angle tuning a birefringent crystal. Refractive index of a birefringent crystal is also temperature dependent, and thus stabilized temperature is required for stable phase-matching [36].

Using quasi-phase matching (QPM) [36] is another technique for phase-matching, in which by periodically changing the sign of nonlinearity (d_{eff}), the nonlinear interaction to the wrong direction of conversion, back to fundamental input frequency, does not occur. In such case, there is no real phase-matching and birefringence is not needed. This allows usage of materials where nonlinear susceptibility is high in a direction where critical phase-matching is not possible. However, the materials for which periodical poling is possible are limited. Furthermore, the quasi-phase matching period can be adjusted by temperature, due to thermal expansion and temperature dependent refractive index [18, 36].

The most commonly used second-order nonlinear optical crystals in the bulk form are inorganic crystals such as monopotassium phosphate (KDP) or potassium titanyl phosphate (KTP), ferroelectrics such as lithium iodate ($LiIO_3$) or lithium niobate ($LiNbO_3$),

and the borates such as beta barium borate (BBO) or lithium triborate (LBO) [36, 62]. These meet the requirements for a bulk nonlinear crystal: large effective nonlinear coefficient, broad transparency range, high optical homogeneity, high damage threshold, wide acceptance angle and small spatial walk-off.

2.3.2 Diamond Raman laser as a frequency converter

Raman scattering is an inelastic scattering process where light is scattered by molecules. It was first discovered by C. V. Raman and K. S. Krishnan in 1928 [63]. A schematic presentation of scattering process is shown in Figure 2.10 in which photons can either gain or loose energy proportional to the (rotational-)vibrational energy states of the molecules. These two shifts in energy are called Stokes and anti-Stokes shifts for lower and higher energy, respectively.

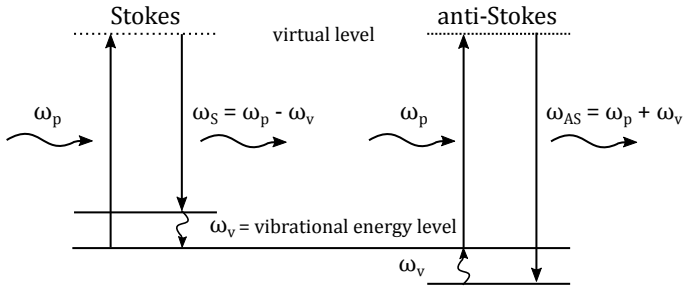

Figure 2.10: Schematic presentation of energy levels for Raman Stokes and anti-Stokes scattering.

After the invention of lasers it was soon realized that under intense laser beams the amount of Raman scattering was several orders of magnitude higher, which lead to the conclusion of stimulated Raman scattering, first described by Y. R. Shen and N. Bloembergen. [64].

In the simplest form, the stimulated Raman scattering can be described as a coupled intensity differential equations [36, 65]

$$\frac{\mathrm{d}I_S}{\mathrm{d}z} = gI_SI_P \tag{2.28}$$

$$\frac{\mathrm{d}I_P}{\mathrm{d}z} = -\frac{\nu_P}{\nu_S}gI_SI_P, \tag{2.29}$$

where I_S and I_P are the intensities at Stokes and pump wavelengths, g is the Raman gain coefficient, and ν_P and ν_S are the frequencies of the pump and Stokes waves. Thus, stimulated Raman scattering is an intensity dependent (or third order) nonlinear process highly dependent on the pump intensity and the Raman gain coefficient.

Raman lasers are a subtype of lasers that use stimulated Raman scattering for amplifying light. There are two major differences to the common lasers: firstly, as Raman scattering is based on weak and "instantaneous scattering process", (energy is not stored in the gain medium,) the Raman medium can only be used with intense pump laser, and secondly, the pump source is not limited to any particular wavelength but only the scattered wavelength is defined by the difference of pump photon energy and Raman Stokes shift.

The are several types of Raman laser ranging from Raman fiber lasers, to gas, liquid, semiconductor and solid-state Raman lasers. The Raman lasers can be pumped either intra-cavity, like typical continuous wave Raman lasers [66, 67], or extra-cavity , like synchronously pumped by mode-locked lasers [68, 69], Q-switched lasers [70, 71], or simple Raman generators [72, 73]. There are even demonstrations of intra-cavity pumped Q-switched microchips [74, 75], however this extends the cavity length dramatically and as it was seen previously this would mean very long pulses. Thus, in this thesis hereinafter, only extra-cavity Raman lasers are considered.

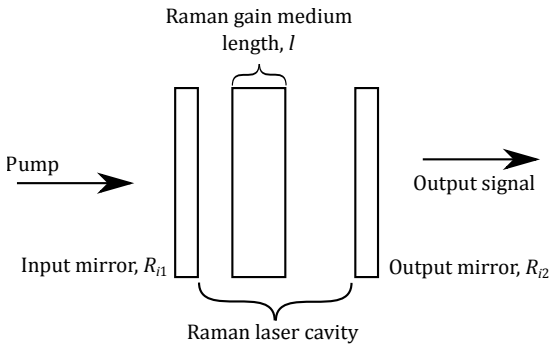

Figure 2.11: A schematic of a extra-cavity Raman laser.

In its simplest form, an extra-cavity Raman laser shown in Figure 2.11 consist of a Raman medium of length l with Raman gain coefficient g_0 between input mirror R_{i1} and output mirror (R_{i2}), where i denotes for i:th Stokes. In such case, the evolution of the Stokes intensities I_i over time can be represented as a set of intensity rate-equations under the uniform intensity approximation of the Stokes beams inside the resonator as follows [76]

$$\frac{\mathrm{d}I_1}{\mathrm{d}t} = \frac{2\nu_1 I_P}{\nu_P \tau_{rt}}(1 - e^{-g_0 I_1 N l}) - \frac{2g_1 l}{\tau_{rt}} I_1 I_2 - \frac{I_1}{\tau_{rt}}(L - \ln(R_{11}R_{22})) + \frac{k_{sp}}{\tau_{rt}} I_P \quad (2.30)$$

$$\frac{\mathrm{d}I_2}{\mathrm{d}t} = \frac{2g_2 l}{\tau_{rt}} I_2(I_1 - I_3) - \frac{1}{\tau_{rt}} I_2(L - \ln(R_{21}R_{22})) + \frac{k_{sp}}{\tau_{rt}} I_1 \quad (2.31)$$

$$\frac{\mathrm{d}I_3}{\mathrm{d}t} = \frac{2g_3 l}{\tau_{rt}} I_3 I_2 - \frac{1}{\tau_{rt}} I_3(L - \ln(R_{31}R_{32})) + \frac{k_{sp}}{\tau_{rt}} I_2, \quad (2.32)$$

where ν_i are the pump and Stokes wave frequencies, I_P is the pump intensity, τ_{rt} is the cavity round trip time, N is 1 or 2 for single- and double-pass pumping, L is the round trip dissipative loss inside the resonator and k_{sp} is the spontaneous Raman scattering factor. The Raman gain coefficient factors are defined by

$$g_i = \frac{\nu_{i-1}}{\nu_i} g_{i-1}, \quad (2.33)$$

for which g_0 is the Raman gain coefficient at pump wavelength. The spontaneous Raman scattering factor is further defined as $k_{sp} = 2lK_{sp}$ where K_{sp} is also called spontaneous Raman scattering factor independent of the Raman medium length l, but is dependent on laser geometry [65]. Finally, it should be noted that this model does not account for the terms producing off-axis high order Stokes components nor four-wave mixing processes [65, 76].

Despite the generalizations and simplifications in these intensity rate equations, Ding *et al.* [76] found that they give a good approximation for the case of low gain $G_i =$

$g_i I_{P,max} l_L < 4$ and long pump pulse $N = \tau_p/\tau_{rt} > 50$. In this thesis, the peak gain exceeds this limit at high pump powers, and the pump pulses are rather short in respect to cavity round trip time (N is 3–13 in this thesis). Thus, the model is used only as simple model to understand the basic behavior and calculations are made for indicative purposes only.

In this thesis, the goal is to use Raman lasers only for Stokes waves but as Shen *et al.* noted already in 1965 that "*the real situation is however that the anti-Stokes wave is always present and coupled to the Stokes and vibrational waves. Even in a Raman laser, a small amount of anti-Stokes wave is always dragged along with the Stokes wave in forward direction*" [64]. Thus, anti-Stokes emission was observed for all studies later presented in Chapter 3, however, with very small output power in comparison to Stokes power.

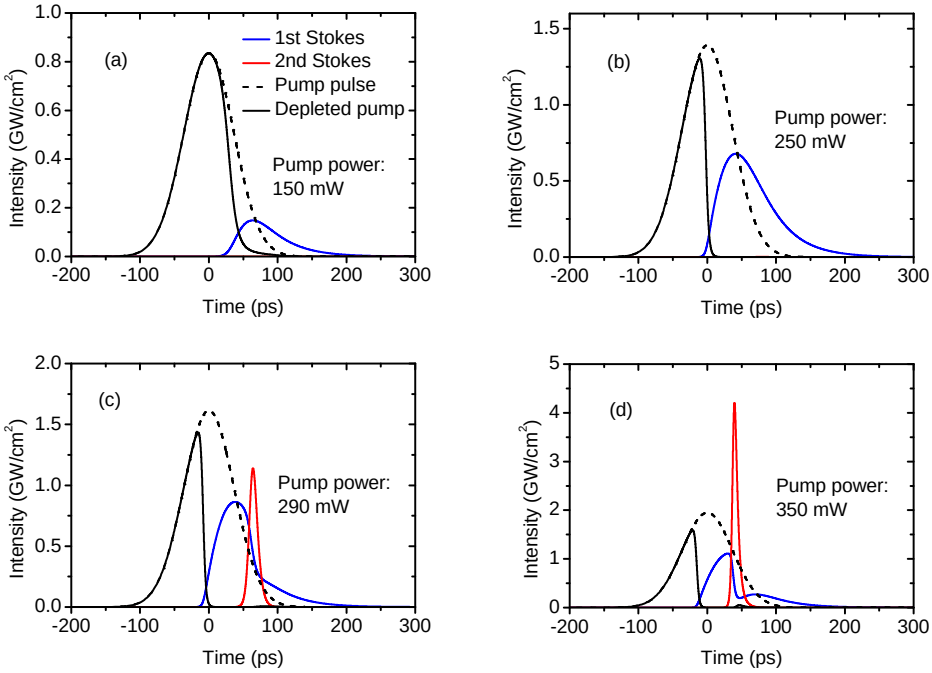

Figure 2.12: Simulated pulse formation in a diamond Raman laser using the intensity rate equations of (a) above 1st Stokes threshold intensity, (b) below 2nd Stokes threshold intensity, (c) above 2nd Stokes threshold intensity and (d) at high pump intensities. Values used in simulation: $\tau_p = 86$ ps, $l_L = l_R = 0.05$ cm, $n = 2.42$, $g_0 = 15$ cm/GW, $g_1 = 8.3635$ cm/GW, $R_{12} = 0.82$, $R_{11} = 0.99$, $R_{22} = 0.15$, $R_{21} = 0.25$, $L = 5 \cdot 10^{-04}$, $N = 2$, $k_{sp} = 10^{-08}$, $\nu_L = c/532$nm, $\nu_1 = c/573$nm, $\nu_2 = c/620$nm, $t_{rt} = 8.1$ ps.

A typical theoretical Stokes pulse formation, or intensity oscillation, of a Raman laser is shown in Figure 2.12 at different pump powers. The corresponding output power, conversion efficiency and pulse duration are presented in Figure 2.13 as a function of pump power. The pulse formation of Figure 2.12 can be understood in 4 steps. 1) At the 1st Stokes threshold the 1st Stokes pulse is formed at the end of the pump pulse and the conversion efficiency is low. 2) When pump power is increased, the 1st Stokes threshold is reached earlier in respect to the pump pulse and the 1st Stokes pulse has longer time to gain power, and thus the 1st Stokes pulse duration gets (slightly) longer. 3) When

2nd Stokes threshold is exceeded, more power is converted from 1st to 2nd Stokes and the 1st Stokes conversion efficiency starts to drop: while the 2nd Stokes converts power from 1st Stokes the 1st Stokes pulse is effectively shortened and distorted. 4) At very high intensities the competing 1st and 2nd Stokes intensities start to oscillate and the pulse shape becomes asymmetric. In this model, appearance of 3rd Stokes was neglected.

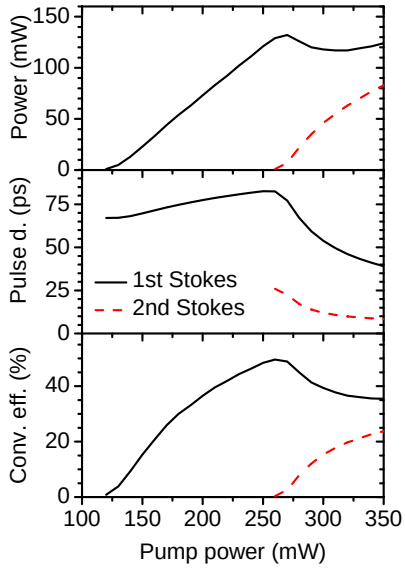

Figure 2.13: Simulated output power, pulse duration and conversion efficiency. Note: Model is not accurate for high gain/power and thus calculated pulse duration of 2nd Stokes is shorter than in reality.

The most commonly used solid Raman gain materials are crystals such as diamond, silicon, $LiIO_3$, $Ba(NO_3)_2$, $KGd(WO4_4)_2$, $BaWO_4$ and YVO_4 [77]. Between these materials, diamond is superior material for high power Raman lasers due to its outstanding properties such as high thermal conductivity, high damage threshold, wide transparency range, low loss, low thermal expansion coefficient and most importantly high Raman gain coefficient of 42 cm/GW ([111] direction at 532 nm) [78] and large Raman shift of 1332 cm^{-1} [77].

3 Experimental Work and Results

The experimental work carried out in this thesis, consists of three main components: the master-oscillator, power amplifier and frequency conversion. The function of the master-oscillator is to produce short pulses with reasonably small pulse energy, which can be sustained by the SESAM. The function of the amplifier is to boost the pulse energy to a level required by the application. The addition of the frequency conversion unit allows extending the wavelength coverage to spectral regions that are not accessible by direct emission of the master oscillator.

In this chapter, I will describe the experimental results obtained for each of the three main components of the system. The master-oscillator is the most important part of the system in order to meet the desired specifications as it allows the generation of short optical pulses. The work was initially started with 1064 nm master-oscillator with the target to obtain sub-100 ps pulses. Later, the work was extended to 1342 nm, with similar target for pulse duration. The results obtained from these experiments are described in the section "3.1 Master-oscillators".

There are a number of reasons for the use of a separate power-amplifier is advantageous with the microchip master-oscillator. First of all, the mode area on the microchip has to be small in order to maintain single transversal mode operation. Due to the demand for short output pulse, also the thickness of the crystal is limited. Thus, the overall mode volume in the microchip laser is small and the possibilities for power scaling are very limited. Therefore, an external power-amplifier is an excellent option for power scaling. This system architecture also allows independent tuning of the repetition rate and laser power. Here, we used Nd:YVO_4 bulk amplifiers both for 1064 nm and 1342 nm signal amplification, due to the high emission cross section and naturally coinciding gain bandwidth. The results obtained from the amplifier experiments are described in section "3.2 Power amplification".

The combination of a good master-oscillator and power-amplifier offers the desired pulse duration and power level at a fixed wavelength. Different wavelength conversion schemes, such as second, third and fourth harmonic generation, were used to provide more degree of freedom to move in the spectral domain. The results from the harmonic generation are presented in section 3.3. While the harmonic generation offers an excellent way to access 532 nm and shorter wavelengths, it has not been straightforward to generate short pulses at longer wavelengths (550 – 700 nm), because the 1342 nm master-oscillator could not meet the sub-100 ps target. Therefore, we started to seek for alternative technical approaches, which could utilize the 1064 nm and 532 nm system as an "engine" for generating longer wavelengths (573 nm and 620 nm). For this purpose we decided to use diamond Raman laser pumped by 532 nm/1064 nm pulses. The results from the diamond Raman laser experiments are presented in section 3.4 "Diamond Raman lasers". The

roadmap for wavelengths obtained in this thesis and corresponding frequency conversions are shown in Figure 3.1

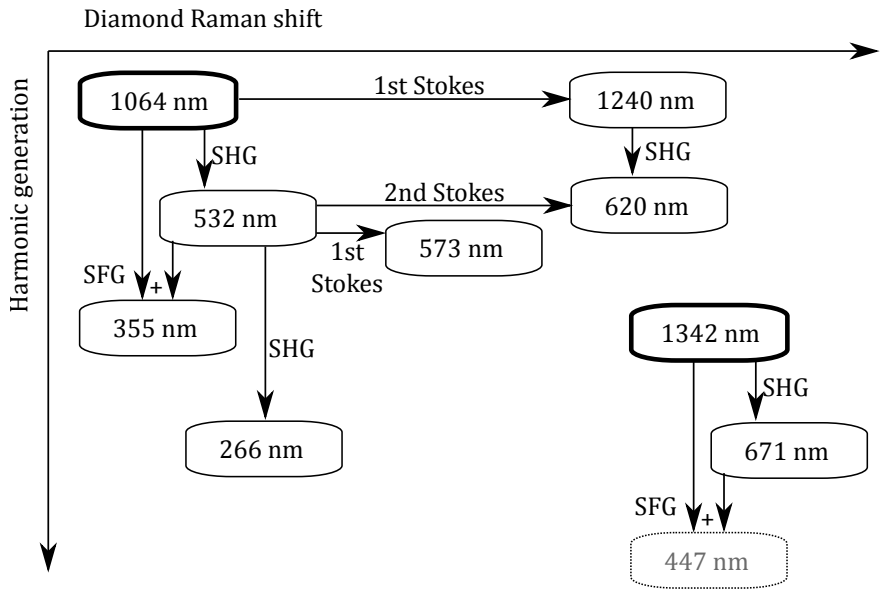

Figure 3.1: Roadmap for frequency shifted wavelengths obtained from primary sources at 1064 nm and 1342 nm. SHG: Second harmonic generation, SFG: sum frequency generation. Not counting the higher order Stokes and anti-Stokes shifts observed. Dashed line: work planned, but not carried out so far.

3.1 Master-oscillators

The master oscillators were build using SESAMs at 1064 nm and 1342 nm. In general, the microchip architecture consisted of a 100 – 200 µm thick planar Nd:YVO_4 crystal bonded to a SESAM. The laser cavity was formed between a partially reflective output coupler coating R_{OC} deposited on the crystal surface and a highly reflective semiconductor Bragg mirror in the SESAM. In the case of the 1342 nm samples, a pump reflecting coating (R > 90% at 808 nm and highly transparent at lasing wavelength) was deposited on the SESAM surface, to avoid any residual pump absorption in the SESAM. After being coated, the SESAM was attached to the vanadate crystal. Finally, the laser chips were glued to aluminium sub-mounts. In the laser setups, the sub-mounts were clamped to larger heat sinks. The pump sources in all cases were commercial fibre-coupled 808 nm laser diodes from which the light was focused into about 70 µm diameter spot on the laser chips. A photograph of two microchips on aluminium sub-mounts is shown in Figure 3.2.

A typical master-oscillator setup is shown in Figure 3.3. The system consists of a 808 nm fiber-coupled pump diode, collimating lens, polarization selective optics, dichroic mirror, pump focusing lens and the microchip laser. The function of the dichroic mirror is to separate spatially the pump light and the signal. Polarizing optics (polarizing cube and half-wave plate) are used to match the pump polarization along the c-axis of the gain crystal, providing the highest pump absorption.

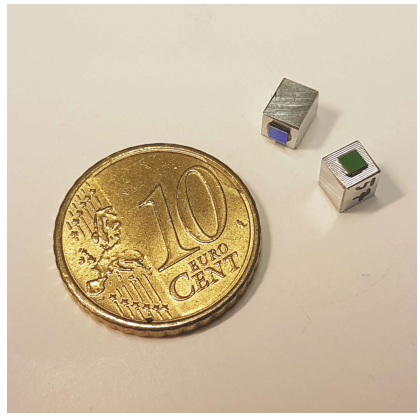

Figure 3.2: Two microchips mounted on aluminium sub-mounts and a 10 cent coin for scale.

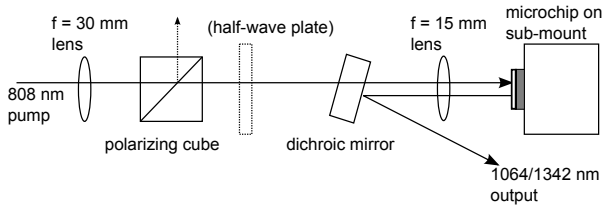

Figure 3.3: A schematic of a typical microchip setup and a pump configuration [P1].

In this work, the output pulse durations were measured with a commercial autocorrelator (Femtochrome FR-103WS), having a scan range of about 400 ps. Typical autocorrelation traces at 1064 nm and 1342 nm are shown in Figure 3.4a. Gaussian fitting function was used for the autocorrelation traces, yielding a value of 102 ps at 1064 nm and 204 ps at 1342 nm.

The longer pulse duration at 1342 nm is explained by two main reasons: longer gain crystal and lower modulation depth of the SESAM. As indicated by equation (2.14) in the theory part, the pulse duration depends linearly on the cavity length and absorber modulation depth. Due to lower emission cross section at 1342 nm, a thicker gain crystal and lower modulation depth of the SESAM is needed to overcome the lasing threshold. Thus, the pulse duration at 1342 nm is not as short as pulse duration at 1064 nm, and the sub-100 ps target was not met at this wavelength. However, the pulse duration of 204 ps at 1342 nm is the shortest reported pulse duration at this particular wavelength from a Q-switched microchip laser. For a point of comparison, typical microchip parameters and output parameters at 1064 nm and 1342 nm are summarized in Table 3.1.

In addition to short pulse duration, a narrow spectral width (<0.1 nm) of the laser is also an important parameter for some applications, such as time-gated Raman spectroscopy, targeted in this work. Due to short cavity length, the microchip lasers presented here, are intrinsically single-frequency lasers. This property arises from the fact that the gain bandwidth is narrower than spacing between two adjacent Fabry–Pérot cavity modes (i.e. the free spectral range of the Fabry–Pérot resonator, eq. (2.1)). For example, at 1064 nm the gain bandwidth is about 1 nm wide, and the spacing of the Fabry–Pérot cavity modes is about 2.6 nm for a 100 µm thick crystal. Therefore, the gain is able to

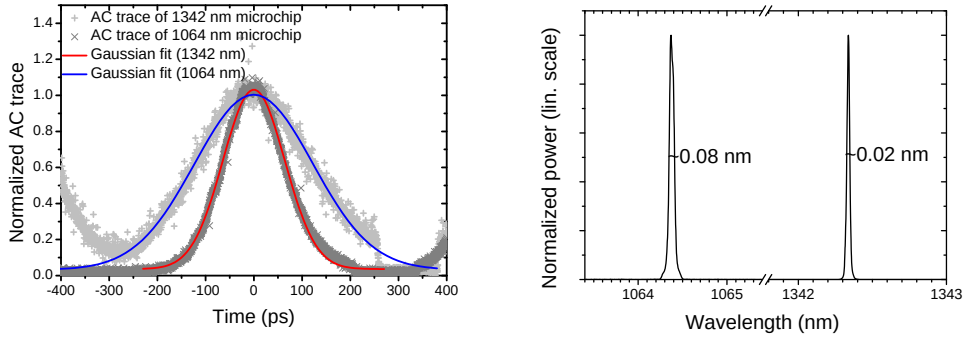

Figure 3.4: (a) Typical autocorrelation traces of microchip outputs and (b) spectra at 1064 nm and 1342 nm, measured with an optical spectrum analyzer having a resolution of 0.02 nm [P1, P3].

support only one longitudinal resonator mode at a time. The spectral width of the laser mode is defined by the finesse and free spectral range of the cavity (see eq. (2.2)), which ensures narrow spectral width below 0.1 nm, with typical output coupler reflectance of about 90%. The output spectra at 1064 nm and 1342 nm, measured with an optical spectrum analyzer with resolution of 0.02 nm, are shown in Figure 3.4b. The spectral widths were 0.08 nm and 0.02 nm, for 1064 nm and 1342 nm, respectively. The narrower spectrum at 1342 nm is likely explained by the lower gain and smaller free spectral range.

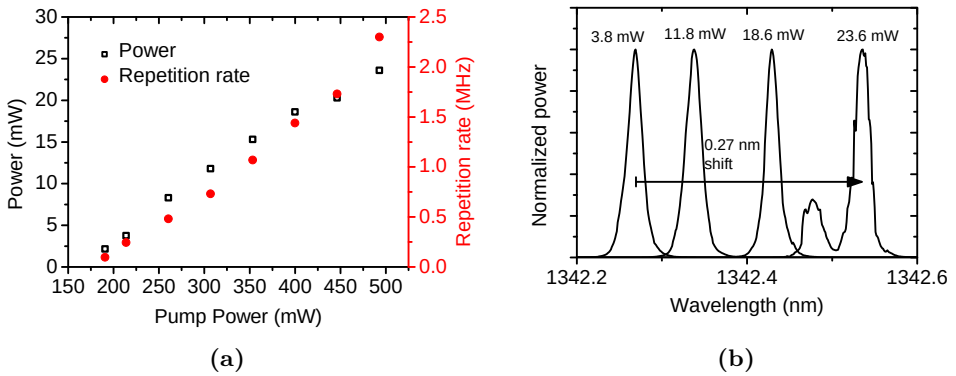

Figure 3.5: (a) Output power and repetition rate of a 1342 nm Q-switched microchip laser versus pump power and (b) spectra at different output powers [P1].

Figure 3.5a reveals the output power and the repetition rate of a Q-switched 1342 nm microchip laser as a function of the pump power. The pulse formation – pulse duration and energy – are mostly defined by the population inversion and modulation depth of the SESAM, independent of the pump power. Consequently, the average output power and the repetition rate are both linearly dependent on the pump power, as seen in Figure 3.5a. In other words, higher pumping leads to higher repetition rate and average power, while the pulse energy and pulse duration remain nearly constant. The output spectra corresponding to different power levels of Figure 3.5a, are presented in Figure 3.5b.

The observed red shift with increasing power is due to heating of the gain chip, leading to shift of the cavity resonance by the amount of thermal expansion. In this particular case, single-frequency operation is demonstrated up to 18.6 mW average power and at 23.6 mW multiple transversal operation is indicated by the appearance of a side mode in the spectrum.

Table 3.1: A comparison of the typical microchip parameters and output parameters at 1064 nm and 1342 nm.

Wavelength	nm	1342	1064
Publ.		P1	P3
Microchip parameters:			
Gain thickness	µm	200	100
R_{OC}	%	86	90
Pump reflector @ 808 nm	%	>90	no
nro. of QWs		2×3	-
Modulation depth[1]	%	4	8−10
Microchip results:			
Wavelength	nm	1342	1064
Spectral width	nm	0.02	0.08
Pulse duration	ps	204	102
Average power[1]	mW	1.04	10
Repetition rate	kHz	100	100
Pulse energy	µJ	0.01	0.1
Peak power	kW	0.05	0.92

[1] Modulation depth is estimated from as-grown samples, i.e. with SESAM-air interface.

To summarize, the SESAM Q-switched 1064 nm microchip lasers fulfill the specifications for narrow spectrum, short pulse duration and low repetition rate, set for the master-oscillator. In case of 1342 nm master-oscillator, the sub-100 ps target pulse duration was not met, but the obtained 204 ps pulses still set the record for shortest Q-switched pulses at this wavelength, and could be useful for many applications. The Q-switched microchip features and obtained output parameters are summarized in Table 3.1 for both wavelengths.

3.2 Power amplification

As mentioned previously, the pulse energy and pulse duration of the Q-switched master-oscillator remain nearly constant regardless of the pump power. An external power-amplifier allows us to increase the pulse energy and peak power, preferably without affecting the spectrum or pulse width.

There are several amplifier materials and configurations commercially available today. The most commonly used materials include doped crystals and glasses, doped optical fibers (glass) and optical semiconductors. Out of these, semiconductors are a poor choice of materials for amplifying low repetition rate lasers, due to their short upper state lifetime, typically in the range of 1−2 ns, which prevents them from storing energy between the pulses.

Ytterbium-doped double-clad fiber amplifiers have long upper state lifetime and can provide very high gain, high efficiency and high output powers up to the multi-kW range [79]. However, the small mode field diameter and high pulse intensity make this approach prone to nonlinear optical effects such as self-phase modulation and stimulated Raman scattering, which may negatively affect both spectral and temporal properties of the pulses [80].

In contrast, in bulk crystal or glass amplifiers the mode area can be up-scaled avoiding the nonlinear effects. However, doped crystal materials have very limited gain bandwidth, due to which only Nd:YAG and Nd:YVO_4 are potential options for 1064 nm and Nd:YVO_4 for 1342 nm. Out of these two materials, YAG has higher thermal conductivity and higher saturation fluence [81], which makes it suitable for high power amplification. YVO_4 on the other hand, has higher emission cross section [57], which makes it better suited for small signal amplification, pursued here.

Doped crystal (and glass) amplifiers can be arranged in a number of configurations including traditional bulk, slab and rod arrangements, for example. Slab and rod amplifier are essentially bulk amplifiers in which the amplifier geometry may provide improved heat transfer and/or pump beam guiding. Such amplifiers could be highly advantageous for short pulse amplifications, especially with very high pulse energies [22, 82–84]. However, here we chose to use traditional Nd:YVO_4 bulk crystal amplifiers as the minimum viable solution, having simple pump arrangement, sufficient amplification, low cost and wide commercial availability.

In this thesis, two power amplifier setups were built, one for 1064 nm and one for 1342 nm. The basic principles of the two setups are the same with the major difference that the 1342 nm system included two stages of amplification, due to weaker emission cross section. The schematic presentations of the setups are shown in Figure 3.6.

Both amplifiers incorporate 5–6 mm long, 0.5%-doped Nd:YVO_4 crystals with c-axis parallel to master-oscillator polarization, pumped by 808 nm fiber coupled diode lasers (fiber core diameter 105 µm, NA 0.22). The front surfaces of the amplifier crystals were anti-reflection coated for 808 nm and laser signals. The back surfaces were coated for high reflection at laser wavelength and high transmission at 808 nm, while 1342 nm crystals also had high transmission for 1064 nm. The front surface was also wedged at 2-degree angle to prevent lasing in the amplifier. The laser beam diameters in the amplifier crystals were about 100 µm, which closely correlated with the 808 nm pump spot diameters. The amplifier crystals were wrapped in indium foil and clamped to Peltier cooled heat sinks maintained at 20 °C temperature.

The double-pass amplifier setups shown in Figure 3.6 include optical circulators, formed by half-wave plates, polarizing beam splitter cubes and Faraday rotators, where the light is passed around to another stage of double-pass amplifier and finally to the output (at 1342 nm setup), or directly to the output (at 1064 nm setup). The setups also contain additional isolators to prevent feedback from the amplifier to the microchip laser and from the output back to the amplifiers. The two-stage amplifier at 1342 nm also contains an additional long-pass filter to filter out 1064 nm signal and therefore prevent lasing at 1064 nm.

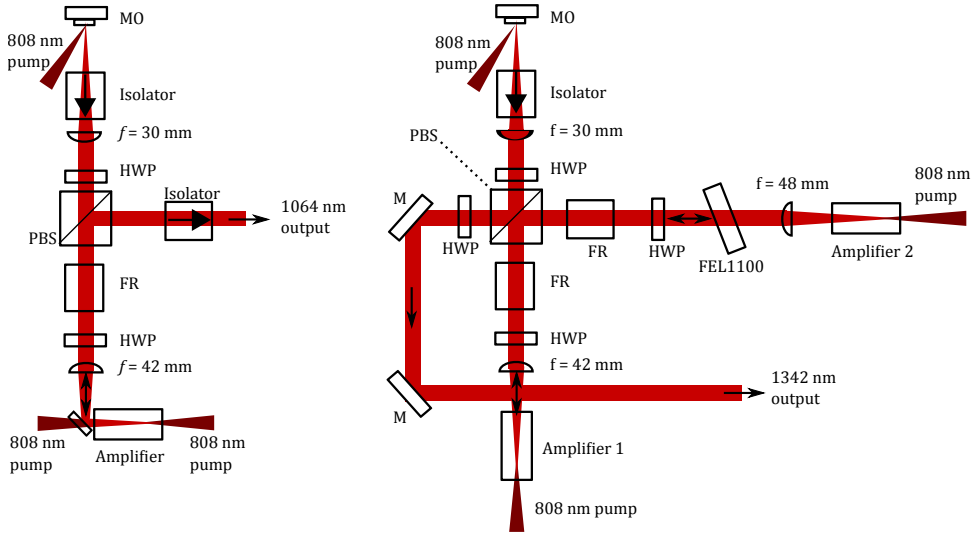

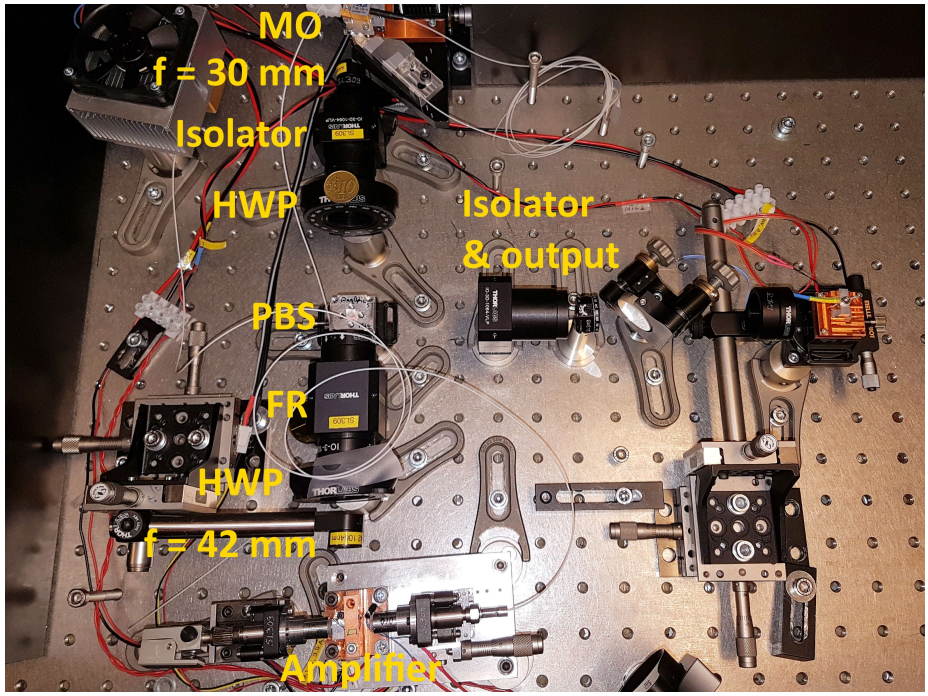

Figure 3.6: Top: Schematics of amplifier setups at 1064 nm and 1342 nm [P2, P3]. MO: master-oscillator, HWP: half-wave plate, PBS: polarizing beam splitting cube, FR: Faraday rotator, FEL1100: 1100 nm long-pass cut-off filter, M: (silver) mirror. Bottom: Generic photograph of the 1064 nm master-oscillator power-amplifier setup on optical table.

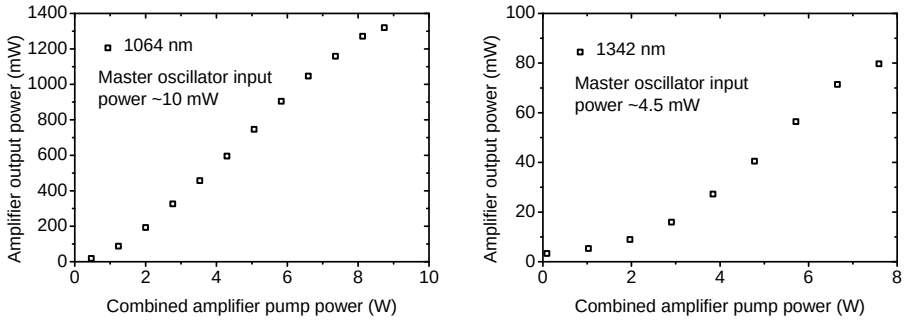

(a) **(b)**

Figure 3.7: Amplifier output powers for 1064 nm (a) and 1342 nm (b) setups versus combined pump power at 808 nm [P2, P3].

With a 1064 nm input power of ∼10 mW at 100 kHz, a maximum output power of 1.32 W was reached at 8.7 W of incident pump power (combined from two pump diodes), as shown in Figure 3.7a. At 1342 nm, 80 mW of output power was reached at pump power of 7.6 W, with input power of ∼4.5 mW at 444 kHz (Figure 3.7b). For comparison, at 7 W pump power level the 1064 nm signal was amplified by factor of 110× from 10 mW to 1100 mW, while the 1342 nm signal was amplified only 17× from 4.5 mW to 75 mW. Also, both pulse duration and spectral width in both cases were measured before and after amplifiers and no changes were observed, in either case.

To summarize, the obtained results clearly indicate that the 100-ps pulses at 1064 nm can be amplified to sufficiently high power without penalty to pulse duration or spectral width. The 1342 nm system could just barely meet the power targets, but the amplification was significantly smaller in comparison to 1064 nm, and also the system was far more complex.

3.3 Second harmonic and sum frequency generation

Many high efficiency solid state laser materials, such as Nd, Yb, Er, Ho, Tm-doped crystals and glasses, emit in the infrared region, and can be pumped with efficient, low-cost diode lasers. The number of directly visible emitting solid state laser materials, such as Pr-doped crystals and Ruby, is very limited. They also require visible pump sources that are not as mature and widely available as infrared-diodes. Due to these reasons the visible and UV regions are commonly accessed by harmonic frequency conversion of infrared lasers.

As discussed in section 2.3, the nonlinear frequency conversion processes are highly intensity dependent and benefit greatly from narrow spectral width of the input signal. In this work, the intrinsically narrow spectrum, short pulse duration and high intensity enable direct frequency conversion in single-pass configuration with high efficiency. Thus, the system used here, avoids the need for intra-cavity frequency conversion and more complex resonant external-cavity frequency conversion [36, 85]. The single-pass frequency conversion units are extremely simple, easy to align and can be cascaded (as modules). Overall, this makes the frequency conversion scheme compact and robust.

Table 3.2: Used harmonic frequency conversion crystals and results.

Harmonic wl.	nm	266	355	532	620	671
Fundamental wl.	nm	532	1064+532	1064	1240	1342
Publ.		P3	P3	P3	-[1]	P2
Properties:						
Material		BBO	LBO	LBO	LBO	PPLN
Type		I	II	I	I	QPM[2]
θ	°	90	42.2	90	85.8	-
ϕ	°	47.7	90	11.6	0	-
Length	mm	5	15	10	10	10
Temp.	°C	25	25	25	25	83.2
d_{eff}	pm/V	1.75	0.54	0.83	0.82	17
Results:						
Wavelength	nm	266	355	532	620	671
Spectral width	nm	-	0.06	0.08	0.11	0.12
Pulse duration	ps	<86	<86	86	46	225
Avg. Power	mW	83	143	720	128	55
Repetition rate	kHz	100	100	100	100	444
Pulse energy	µJ	0.83	1.43	7.2	1.28	0.124
Peak power	kW	>9	>16	79	21	0.52
Conv. Eff.	%	19	13	56	50	69
Input pulse	ps	86	102/86	102	62	326

[1]To be published

[2]Quasi phase-matched (QPM) poling period is 13.5 µm

A typical single-pass frequency conversion scheme consists of a focusing lens, nonlinear crystal, collimating lens and a dichroic mirror that separates the frequency converted signal from the input beam. In this thesis, 2nd, 3rd and 4th harmonic wavelengths were generated from the 1064 nm, and 1342 nm and 1240 nm inputs were both frequency doubled. The 1240 nm signal was generated from a Raman laser discussed in the next section. Schematic presentations of the setups are shown in Figure 3.8 with a photograph

of a typical frequency conversion setup. The details of the nonlinear crystals used are listed in Table 3.2.

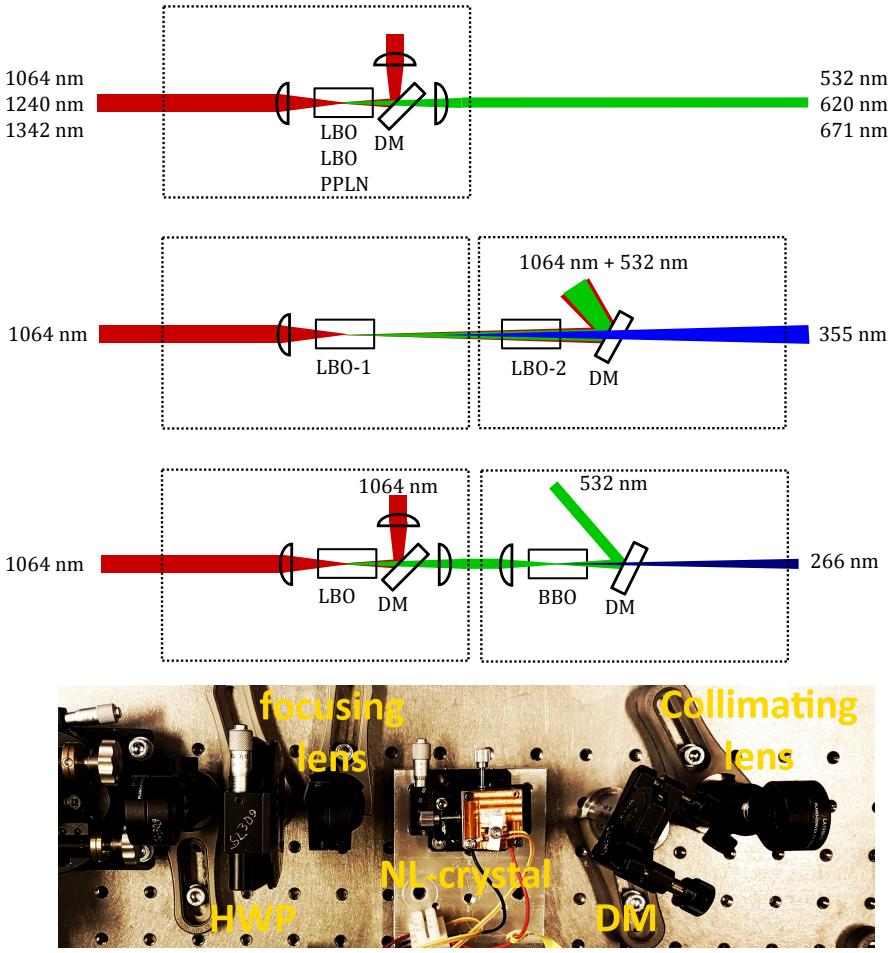

Figure 3.8: Top: Schematic presentations of the harmonic frequency conversion setups, each dashed box presenting one modular step. LBO: Lithium Triborate, PPLN: Periodically Poled Lithium Niobate, BBO: Beta Barium Borate, DM: Dichroic mirror, HWP: Half-wave plate [P2, P3]. Bottom: A generic photograph of a harmonic conversion setup.

The frequency converted powers versus incident power with corresponding conversion efficiencies are presented in Figure 3.9, along with their corresponding spectra and typical beam profiles. The main results, highest power with corresponding conversion efficiency and pulse duration, are also compiled in Table 3.2.

The obtained results show that the >50 mW average power target was reached at all harmonic wavelengths. Also the target for spectral width of less than 0.1 nm was met in all cases, except that at 266 nm spectral width could not be measured with sufficient resolution, due to lack of a suitable measurement device. Conversion efficiency from IR to visible exceeded 50% in all cases. The conversion from 532 nm to 266 nm was 19%, and from 1064+532 nm to 355 nm was about 13%. The lower conversion efficiency at

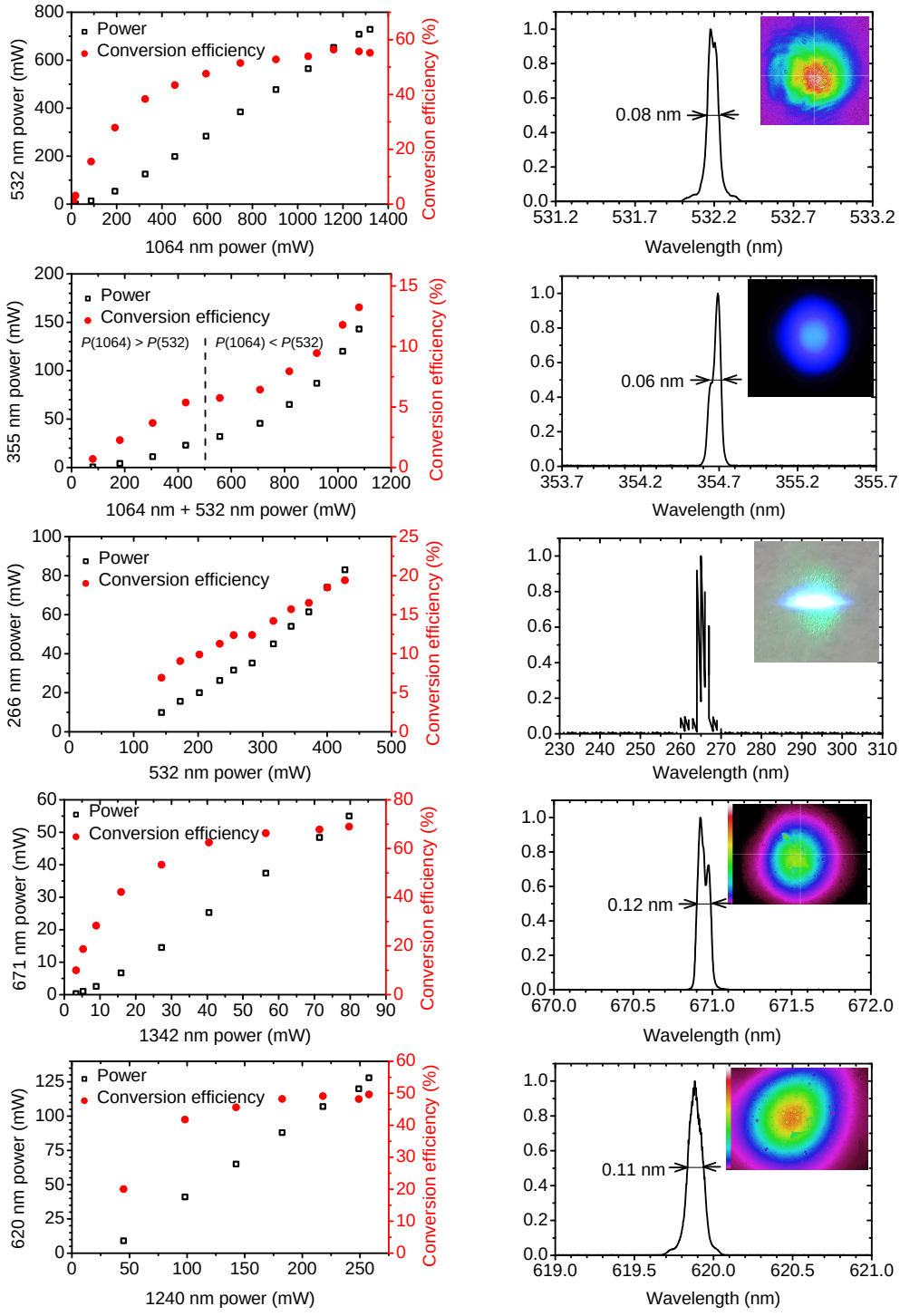

Figure 3.9: Left: Frequency converted powers and conversion efficiencies given as function of input power. Right: Corresponding output spectra and beam profiles (VIS)/pictures (UV). [P2, P3] and 620 nm data to be published.

355 nm was in part due to mismatch in overlap of 1064 nm and 532 nm input signals, both spatially and temporally. At 266 nm the conversion efficiency is in part limited by the large spatial walk-off in the BBO crystal, which limits the crystal length.

To summarize, the combination of SESAM Q-switched microchip master-oscillator, bulk power-amplifier and single-pass harmonic generation in bulk crystal provides an efficient way for generating sub-100 ps pulses at UV and visible parts of the spectrum. The chosen laser architecture is also modular, robust and easy to align, which makes it also interesting for commercial applications.

3.4 Diamond Raman lasers

As shown in the previous section, the generation of harmonic frequencies enables formation of sub-100 ps pulses at 532 nm, 355 nm and 266 nm, however, this technique does not allow us to produce sub-100 ps visible pulses at wavelengths longer than 532 nm. For this reason, the Raman laser approach was used to target the hard-to-reach wavelengths at 570 – 630 nm.

As discussed in section 2.3.2, generation of stimulated Raman scattering is dependent on the Raman gain material, pump wavelength and intensity. Here, diamond was the material of choice, for its superior thermo-optical properties. The absolute Raman gain [78] at 532 nm is more than twice the gain at 1064 nm, thus the first Raman laser experiments were started using 532 nm pumping. Later, also 1064 nm pumping was used.

In total, three different diamond Raman lasers were built, two of which operated at 573 nm (532 nm pump) and one at 1240 nm (1064 nm pump). All systems consisted of a thin planar diamond, coated on both sides to form a simple monolithic plane-plane cavity. The setups contained the pump, a half-wave plate, pump focusing lens, the Raman diamond and an output collimating lens. Different pump focusing lenses were tested in the experiments as the pump intensity significantly affects the pulse duration and generation of higher order Stokes lines. A photograph of a typical Raman laser setup is shown in Figure 3.10. The details of the diamonds and coatings are summarized in Table 3.3 and a microscope picture of a diamond Raman laser sample is shown in Figure 3.11.

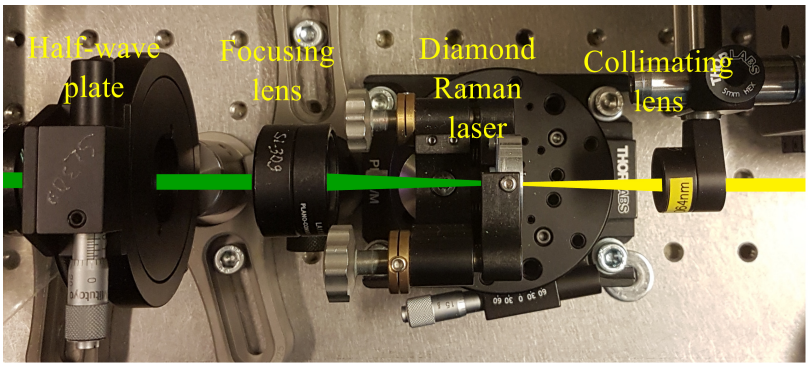

Figure 3.10: A photograph of a typical Raman laser setup.

The Diamond-1 and Diamond-2 were provided by Prof. Alan Kemp's group from the University of Strathclyde, Glasgow, Scotland, and they were both designed for pumping at 532 nm.

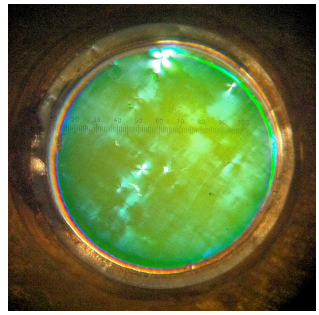

Figure 3.11: A polarizing microscope picture of a Raman diamond. The color changes in the diamond correlate to changes in birefringence. Aperture diameter in the picture is about 4 mm.

Table 3.3: Input and output coating reflectance (%) of the diamond Raman lasers. HR: high reflectance (>99.6%).

	Diamond-1	Diamond-2	Diamond-3
Pump	532 nm	532 nm	1064 nm
Thickness	0.5 mm	2 mm	0.5 mm
Publ.	P4	To be publ.	To be publ.
	R_{i1}/R_{i2}	R_{i1}/R_{i2}	R_{i1}/R_{i2}
1st anti-Stokes	23/35	23/35	52/44
Pump	18/HR	18/HR	0.1/HR
1st Stokes	HR/82	HR/60	HR/52
2nd Stokes	15/25	15/15	3/1.2

With Diamond-1 (thickness 0.5 mm) we achieved up to 180 mW of average power at 573 nm 1st Stokes with conversion efficiency of 47.6% using $f = 75$ mm pump focusing lens (⌀47 µm pump spot), while the highest conversion efficiency of 52% was achieved at 157 mW of average power. At high powers the conversion efficiency is limited by the appearance of 2nd Stokes output as seen in Figure 3.12. The corresponding pulse durations varied around 56 – 76 ps, as seen in Figure 3.12. By scaling up the pump spot size, with $f = 100$ mm lens (⌀62 µm pump spot) the conversion efficiency was slightly reduced, but the pulse durations decreased to 36 – 39 ps. A typical output spectrum is shown in Figure 3.12 and has a spectral width of 0.05 nm. The diamond was also tested using $f = 50$ mm pump focusing lens (⌀31 µm pump spot) and up to 16.4 mW of 2nd Stokes emission was observed at 620 nm and less than 2 mW of 1st anti-Stokes at 497 nm was observed. In other words, smaller pump spot size generates more higher order Stokes and anti-Stokes emission (clearly seen in Table 1 at [P4]).

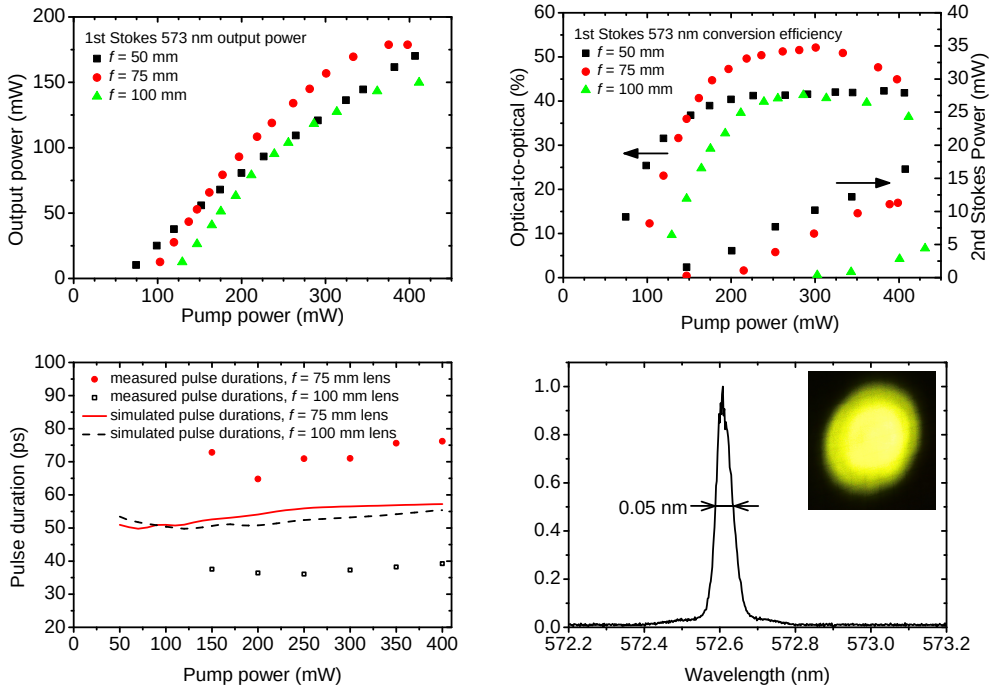

Figure 3.12: Top-left: Output power of the Diamond-1. Top-right: Conversion efficiency from 532 nm pump to 1st Stokes and 2nd Stokes output power. Bottom-left: Measured and simulated pulse duration. Bottom-right: 1st Stokes output spectrum and a photograph of the output beam. (0.5 mm diamond Raman laser at 573 nm with various pump focusing lenses). [P4]

Studies with Diamond-2 (thickness 2 mm) were done under intense pump focusing with a $f = 19.1$ mm lens (⌀12 µm pump spot). High pump intensity lead to efficient 2nd Stokes output up to 62 mW average power with 18% conversion efficiency (pump to 2nd Stokes), while 58 mW (17%) was generated at the 1st Stokes line. The output power curves can be seen in Figure 3.13. The cascading effect to 2nd Stokes output can be clearly seen reducing the 1st Stokes efficiency, while the overall conversion efficiency keeps increasing, and reduced only at high powers. The appearance of 2nd Stokes output also makes the 1st Stokes pulse asymmetric as can be seen in autocorrelator traces in Figure 3.13. This is a results, of conversion to 2nd Stokes from the trailing edge of the 1st Stokes pulse, as predicted in theory (Figure 2.12). High intra-cavity intensity of the 1st Stokes also creates a very short and intense 2nd Stokes pulse down to 24 ps with 10 mW average power, being the shortest pulse duration achieved in this work.

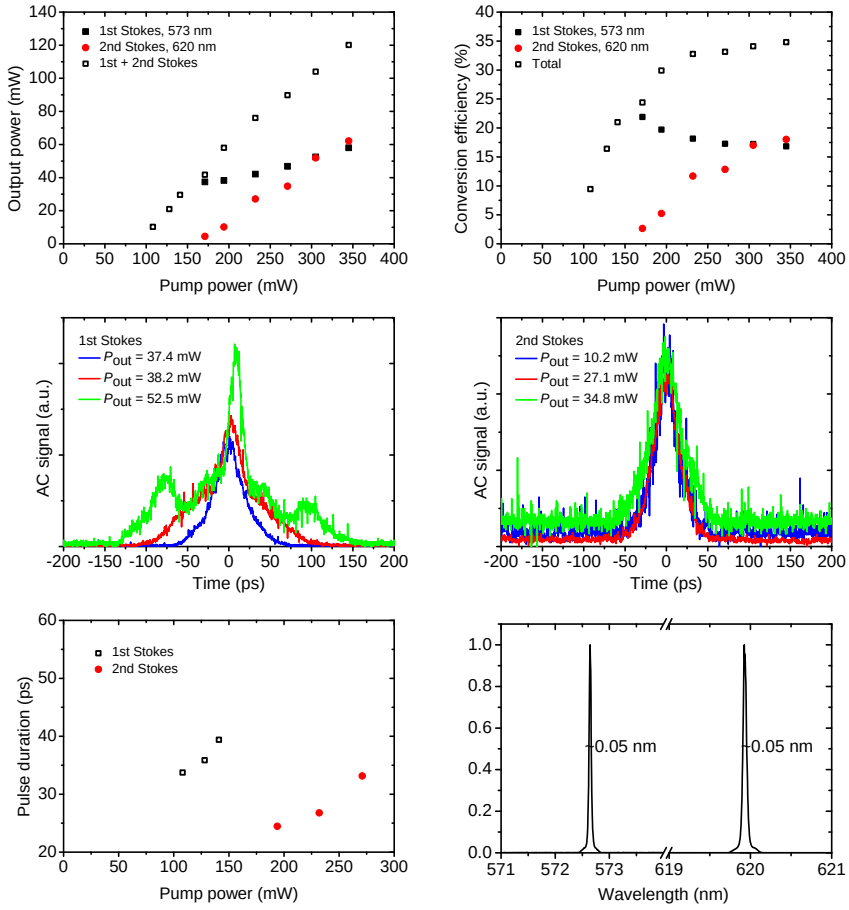

Figure 3.13: Output characteristics of Diamond-2. Top-left: Output power. Top-right: Conversion efficiency from 532 nm pump to 1st Stokes and 2nd Stokes output power. Middle-left: Autocorrelation (AC) signal of the 1st Stokes output. Middle-right: Autocorrelation (AC) signal of the 1nd Stokes output. Bottom-right: Measured pulse durations of 1st and 2nd Stokes output. Bottom-right: 1st and 2nd Stokes output spectra. (2 mm diamond Raman laser at 573 nm and 620 nm). To be published.

This work was continued with a target to extend the picosecond diamond Raman lasers to 1240 nm by 1064 nm pumping. For this purpose, coatings were deposited on Diamond-3 (thickness 0.5 mm) to provide proper reflectance for pump and signal. The effect of the output coupler reflectance to the pulse duration and conversion efficiency was first simulated using the intensity rate equations (2.30)–(2.32). The results of the simulation are shown in Figure 3.14, and suggest that there is a trade-off between the shortest pulse duration and conversion efficiency. Here, the emphasis was put on short pulse duration and about 50% reflectance at 1240 nm was chosen for the output coupler. The 50% reflectance also gives an options to increase the reflectance later by depositing more Bragg reflector layer pairs to the mirror structure, if necessary. The aim was also to suppress the higher Stokes and anti-Stokes lines by minimizing the mirror reflectances at these wavelengths. The deposited coating reflectances are given in Table 3.3.

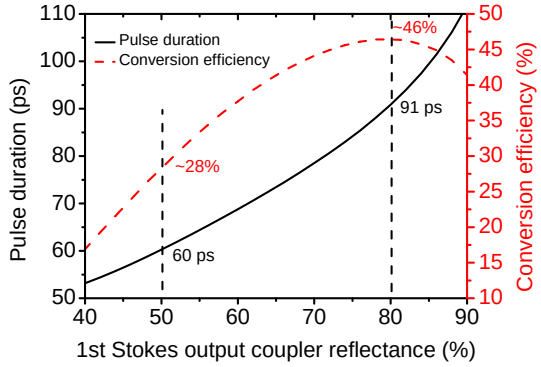

Figure 3.14: Simulated 1st Stokes pulse duration and conversion efficiency versus output coupler reflectance.

The Diamond-3 operated at 1240 nm and the pump was focused with a $f = 48$ mm lens, creating spot of 30 µm in diameter. Up to 246 mW of 1st Stokes output power was achieved with pulse duration of 61 ps, and 25% conversion efficiency. The pulse duration was found to gradually increase, being as short as 41 ps at 45 mW output power. At high powers also up to 3rd Stokes and down to 3rd anti-Stokes emission lines were observed, however the powers were only some hundreds of µW at higher order Stokes and anti-Stokes lines, and at best few mW at 2nd Stokes lines. A typical output spectrum is shown in Figure 3.15 and has a spectral width of 0.06 nm.

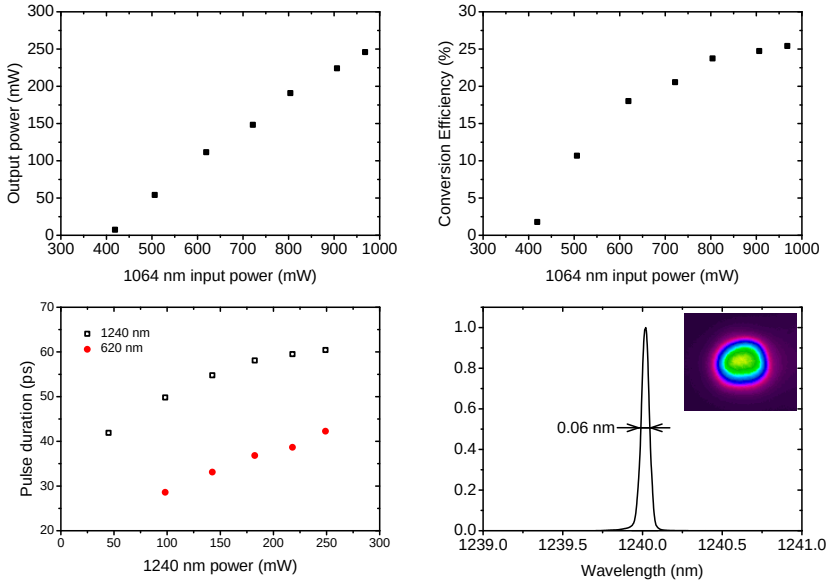

Figure 3.15: Top-left: 1240 nm output power given as function of 1064 nm pump power (Diamond-3). Top-right: Conversion efficiency from 1064 nm to 1240 nm. Bottom-left: Measured pulse durations at 1240 nm and frequency doubled 620 nm. Bottom-right: 1st Stokes output spectrum and an output beam profile. To be published.

Table 3.4: Selected results of the diamond Raman lasers.

Diamond-#		1	1	2	2	3
Publ.		P4	P4	To be publ.	To be publ.	To be publ.
Pump wl.	nm	532	532	532	532	1064
Pump f	mm	100	75	19.1	19.1	48
Pump spot	µm	62	47	12	12	30
Stokes #		1st	1st	1st	2nd	1st
Wavelength	nm	573	573	573	620	1240
Spectral width	nm	0.05	0.05	0.05	0.05	0.06
Pulse duration	ps	39[1]	76[1]	34[2]	24[2]	62
Avg. power	mW	143[1]	170[1]	10[2]	10[2]	246
Repetition rate	kHz	100	100	100	100	100
Pulse energy	µJ	1.43	1.7	0.1	0.1	2.46
Peak power	kW	35	21	2.8	4.0	37
Conv. eff.	%	40	50	17	18	25
Input pulse	ps	86	86	86	86	102

[1]Pulse duration and average power given at a point corresponding to conversion efficiency. Shorter pulses are possible at lower power and conversion efficiency.
[2]Shortest measured pulse durations and corresponding average power.

The stimulated Raman scattering can be understood as a 3rd order nonlinear process and the coupling to anti-Stokes wave can be described as a four-wave mixing process. In order to efficiently convert the light to anti-Stokes wave, a proper phase-matching is required [65]. If the diamond Raman laser is in angle in respect to incident pump beam the phase-matching condition is better satisfied. Thus, throughout the measurements, the diamond was kept at near zero angle of incidence to the pump in order to minimize conversion to the anti-Stokes. However, the photograph in Figure 3.16 was taken when the diamond was tilted by 2° with respect to the incoming pump beam to better satisfy the phase-matching condition. Under these pumping conditions, the higher order Stokes modes are non-collinear and are highly asymmetric, as expected [61]. Also, a (weak) ring pattern, formed by unstable cavity, can be seen in the Figure 3.16.

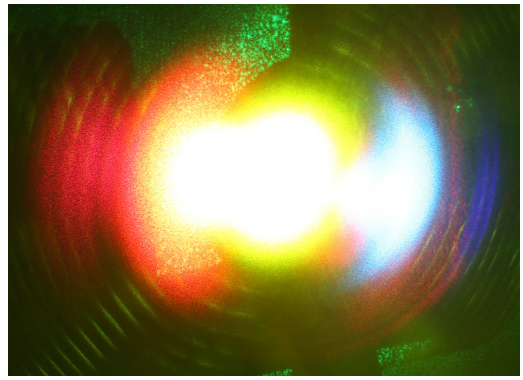

Figure 3.16: A photograph of the Diamond-1 output beam at high pump intensity and small incident angle showing 5 different Stokes/anti-Stokes lines observed [P4].

To summarize, the diamond Raman lasers were found to act as efficient wavelength converters for sub-100 ps Q-switched pulses from 532 nm to 573 nm, and from 1064 nm to 1240 nm. In addition, the diamond Raman laser acted also as an effective pulse shortening element. The conversion efficiency and pulse shortening could be tailored by changing the pump spot diameter and mirror reflectance. A trade-off between maximum pulse shortening and conversion efficiency was observed. At high pump intensities up to 60 mW of 2nd Stokes 620 nm emission was observed. The conversion efficiencies of first and second Stokes could be improved by further optimization of the mirror design.

Short pulse emission at 620 nm was generated via two ways: 1) directly by 2nd Stokes of 532 nm pumped Raman laser, and 2) by frequency doubling 1st Stokes 1240 nm emission from a 1064 nm pumped Raman laser. In the latter case, up to 128 mW of 620 nm emission was generated. The efficiency of 1st Stokes emission at 1240 nm could be potentially further improved by more optimized mirror design, also improving power at 620 nm. In the 532 nm pumped case, the shortest pulses at 620 nm were 24 ps with 10 mW of average power. A clear advantage of the monolithic diamond Raman laser is that it can be added modularly to the system, before or after the harmonic frequency conversion module. In principle, it is also possible to cascade Raman laser modules, in order to suppress the competition of 1st and 2nd Stokes emission. It should be also possible to add/cascade Raman lasers made of different gain materials in order to generate other wavelengths.

4 Conclusion

4.1 Main results and progress beyond the state-of-the art

The main objective of this thesis was to develop sub-100 ps Q-switched microchip lasers for UV, visible and IR regions. The technical approach combined neodymium doped YVO_4 laser crystals and SESAMs as a Q-switching element. This unique combination of high emission cross section solid state gain material and micrometer thick absorber enables the use of very short laser cavity, leading to short output pulse duration.

The SESAM Q-switched 1064 nm microchip lasers fulfilled the specifications for narrow spectrum, short pulse duration and low repetition rate, set for the master-oscillator. In the case of 1342 nm master-oscillator, the sub-100 ps target pulse duration could not be reached, but the obtained 204 ps pulses still set the record for the shortest Q-switched pulses at this wavelength. The outputs from the master-oscillators were amplified without penalty to pulse duration or spectral width. Up to 1.3 W of 1064 nm signal was produced in a single-stage bulk Nd:YVO_4 amplifier. At 1342 nm a dual-stage amplifier system was built producing up to 80 mW of average power, meeting the preset power target relevant for nonlinear conversion and applications. The results obtained at 1342 nm lead to the conclusion that further improvements in pulse shortening and power amplification would face severe limitation owing to low gain available in existing laser crystals.

The excellent results obtained at 1064 nm enabled further harmonic generation in single-pass configuration to 532 nm, 355 nm and 266 nm, with reasonable output power of 720 mW, 150 mW and 83 mW, respectively. A further pulse shortening was also observed in the process of harmonic generation. Following a similar approach, the 1342 nm signal was frequency doubled to 671 nm with 69% efficiency and 55 mW of average output power.

Furthermore, we demonstrated the first picosecond diamond Raman laser with a Q-switched pump laser. The 573 nm Raman laser was pumped by 85 ps pulses at 532 nm and it could produce 39 ps output pulses with 143 mW average power and 40% conversion efficiency. Another diamond Raman laser was demonstrated at 1240 nm, pumped with 1064 nm Q-switched amplified system, delivering 62 ps pulses with 246 mW average power. This laser was also frequency doubled to 620 nm resulting in 46 ps pulse duration and an output power of 128 mW. The red 620 nm wavelength was also achieved as 2nd Stokes emission from 532 nm under intense pumping, and as short as 24 ps pulse duration with 10 mW of average power was achieved. The obtained results show that the diamond Raman laser acts as an efficient wavelength converter and pulse shortening element in the picosecond range.

Table 4.1: Compiled figures of merit of the laser output parameters obtained in this work. Most values listed are the highest output powers achieved and pulse duration corresponds to that of listed power level. From dynamic systems some additional−worthy of mentioning−figures are given.

Publication	Wavelength (nm)	Pulse duration (ps)	Average power (mW)	Pulse energy (µJ)	Repetition rate (kHz)	Peak power (kW)	Method
P3	266	(<86)[1]	83	0.83	100	(>9)[2]	4th harmonic of 1064 nm
P3	355	(<86)[1]	150	1.5	100	(>16)[2]	3rd harmonic of 1064 nm
P3	532	86	720	7.2	100	79	2nd harmonic of 1064 nm
P4	573	39	149	1.5	100	36	1st Stokes Raman, 532 nm pump
P4	573	76	182	1.8	100	22	1st Stokes Raman, 532 nm pump
P4	573	49	167	1.7	100	32	1st Stokes Raman, 532 nm pump
To be publ.	620	24	10	0.1	100	3.9	2nd Stokes Raman, 532 nm pump
To be publ.	620	-[3]	62	0.62	100	-	2nd Stokes Raman, 532 nm pump
To be publ.	620	46	128	1.3	100	26	1st Stokes Raman at 1240 nm and 2nd harmonic
To be publ.	620	33	65	0.65	100	10	1st Stokes Raman at 1240 nm and 2nd harmonic
P2	671	225	55	0.124	444	0.52	2nd harmonic from 1342 nm
P3	1064	102	1320	13.2	100	122	Amplified, direct
To be publ.	1240	62	246	2.5	100	37	1st Stokes Raman, 1064 nm pump
To be publ.	1240	55	112	1.12	100	19	1st Stokes Raman, 1064 nm pump
P1	1342	204	24	0.01	2300	0.05	Direct
P2	1342	326	80	0.8	444	0.52	Amplified, direct

[1]Pulse duration at UV was not measured. Value is expected to be shorter than the fundamental pulse duration.
[2]Calculated with 86 ps pulse duration.
[3]Irregular pulse shape.

The main technical achievements obtained are summarized in Table 4.1. The laser architecture developed exhibits several generic benefits: the master-oscillator is very compact and monolithic, and does not require fine aligning of the cavity elements. The pulse energy can be scaled with a simple and robust power-amplifier, while the repetition rate can be tuned by the master-oscillator. The laser system consists of modular blocks and further power amplification can be done by just adding another stage of amplification to the system. Similarly, new wavelengths can be generated by adding harmonic conversion or Raman laser modules into the system. Such, modular design allows cascaded frequency conversion schemes and may combine Raman lasers and harmonic generation in chosen order. For example, in this thesis 620 nm signal was produced from both frequency doubled 1240 nm Raman laser and directly from a Raman laser pumped by 532 nm. Finally, such modularity makes the overall system easy to align, simple, robust, and build by bulk materials it is low-cost device.

4.2 Future outlook

The future development of sub-100 ps Q-switched microchip systems could take several direction, some of which are summarized below:

1. Development of sub-20 ps pulse sources by optimizing SESAM and Raman lasers
2. Expansion of the wavelength coverage (see Figure 4.1)
3. Power scaling towards 100 µJ pulse energy, and beyond

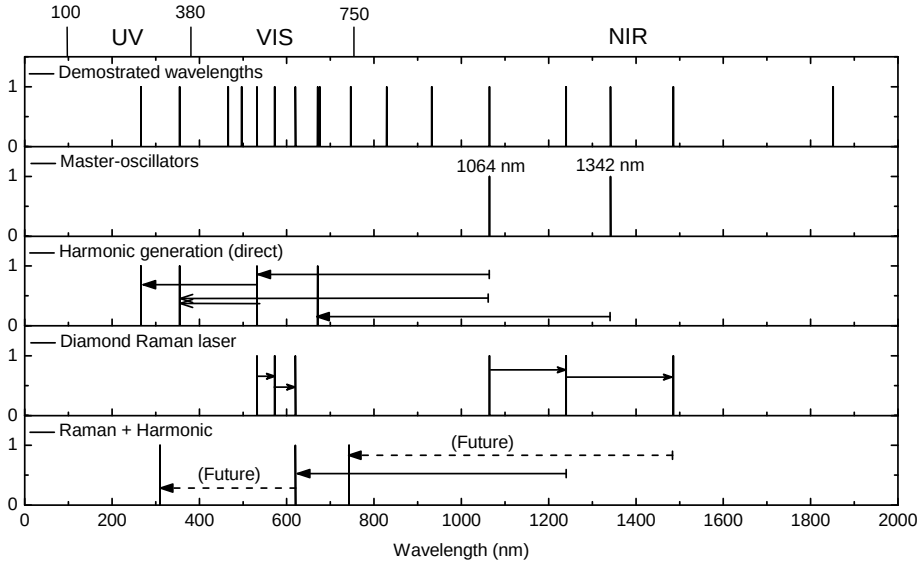

Figure 4.1: Demonstrated spectra, master-oscillator spectra, frequency converted spectra and future work visualized. UV: ultra-violet, VIS: visible and NIR: near-infrared spectral regions.

Related to these generic targets, the shortest optical pulses obtained in this work were 24 ps with 10 mW of average power at 620 nm (2nd Stokes, Diamond-2). It is reasonable to expect that 10−20 ps, or even transform limited 5 ps pulses with spectral width

of 0.11 nm, could be achieved in the future with more optimized system. Simply, by optimizing the coatings of a Raman laser, one could optimize the power at the 1st or the 2nd Stokes line. In the case of 1064 nm pumped diamond Raman laser for example, 1485 nm 2nd Stokes emission could potentially be generated with reasonable efficiency. The 1485 nm could prove useful for application, such as eye-safe high resolution LIDAR. It would also enable generation of frequency doubled signal at 742 nm, which would closely overlap with the operation range of alexandrite lasers. The excellent results obtained at 620 nm suggest that we should be able to generate at least 20 mW of 310 nm UV signal with sub-50 ps pulse duration.

Some short pulse applications require also high average power and high pulse energy. Based on previous reports [86] on short pulse amplification and data sheets of commercially available amplifiers, it seems likely that over 100 µJ pulse energy and over 10 W average power could be achieved using 1 W of 1064 nm input and one stage of power amplification.

Finally, the objectives of this thesis gave very strict requirements (sub-100 ps) for the pulse duration and the gain material was thus limited to Nd:YVO_4 at 1064 nm. However, many applications do not have such stringent requirements for the pulse duration. Thus, the same microchip approach could be incorporated with other laser gain materials reaching more wavelengths, and serving other applications.

Bibliography

[1] O. Svelto, *Principles of Lasers*. Boston, MA: Springer US, 2010. [Online]. Available: http://link.springer.com/10.1007/978-1-4419-1302-9

[2] T. H. Maiman, "Stimulated optical radiation in ruby," *Nature*, vol. 187, no. 4736, pp. 493–494, 1960. [Online]. Available: http://www.nature.com.ezp-prod1.hul.harvard.edu/nature/journal/v187/n4736/abs/187493a0.html%5Cnhttp://www.nature.com.ezp-prod1.hul.harvard.edu/nature/journal/v187/n4736/pdf/187493a0.pdf

[3] H. C. H. Mulvad, E. Palushani, H. Hu, H. Ji, M. Galili, A. T. Clausen, P. Jeppesen, and L. K. Oxenløwe, "Recent advances in ultra-high-speed optical signal processing," in *European Conference and Exhibition on Optical Communication*. Washington, D.C.: OSA, 2012, p. Tu.1.A.5. [Online]. Available: https://www.osapublishing.org/abstract.cfm?uri=ECEOC-2012-Tu.1.A.5

[4] M. C. Rechtsman, "Applied physics: Optical sensing gets exceptional," *Nature*, vol. 548, no. 7666, pp. 161–162, 2017. [Online]. Available: http://www.nature.com/doifinder/10.1038/548161a

[5] W. Koechner, *Solid-State Laser Engineering*, ser. Springer Series in Optical Sciences. New York, NY: Springer New York, 2006, vol. 1. [Online]. Available: http://link.springer.com/10.1007/0-387-29338-8

[6] R. K. Huang, Bien Chann, and P. Tayebati, "Direct diode lasers for industrial sheet metal cutting and welding," in *2014 IEEE Photonics Conference*. IEEE, 2014, pp. 232–233. [Online]. Available: http://ieeexplore.ieee.org/document/6995333/

[7] Y.-Q. Lu and T. Taira, "Introduction: Nonlinear Optics (NLO) 2013 feature," *Optical Materials Express*, vol. 4, no. 1, p. 41, 2014. [Online]. Available: https://www.osapublishing.org/ome/abstract.cfm?uri=ome-4-1-41

[8] D. W. Shipp, F. Sinjab, and I. Notingher, "Raman spectroscopy: techniques and applications in the life sciences," *Advances in Optics and Photonics*, vol. 9, no. 2, p. 315, 2017. [Online]. Available: https://www.osapublishing.org/abstract.cfm?URI=aop-9-2-315

[9] A. Abramovici, W. E. Althouse, R. W. P. Drever, Y. Gursel, S. Kawamura, F. J. Raab, D. Shoemaker, L. Sievers, R. E. Spero, K. S. Thorne, R. E. Vogt, R. Weiss, S. E. Whitcomb, and M. E. Zucker, "LIGO: The laser interferometer gravitational-wave observatory," *Science*, vol. 256, no. 5055, pp. 325–333, 1992. [Online]. Available: http://www.jstor.org/stable/2877074http://www.sciencemag.org/cgi/doi/10.1126/science.256.5055.325

[10] M. Ando et al., "Stable operation of a 300-m laser interferometer with sufficient sensitivity to detect gravitational-wave events within our galaxy," *Physical Review Letters*, vol. 86, no. 18, pp. 3950–3954, 2001. [Online]. Available: https://link.aps.org/doi/10.1103/PhysRevLett.86.3950

[11] J. J. Zayhowski, J. Ochoa, and A. Mooradian, "Gain-switched pulsed operation of microchip lasers," *Optics letters*, vol. 14, no. 23, pp. 1318–1320, 1989.

[12] J. Yang, Y. Tang, and J. Xu, "Development and applications of gain-switched fiber lasers," *Photonics Research*, vol. 1, no. 1, p. 52, 2013. [Online]. Available: https://www.osapublishing.org/prj/abstract.cfm?uri=prj-1-1-52

[13] Y. P. Huang, Y. J. Huang, C. Y. Cho, Y. F. Ma, J. W. Zhang, H. Li, and X. Yu, "High stable electro-optical cavity-dumped Nd:YAG laser," vol. 9, no. 8, pp. 561–563, 2012. [Online]. Available: http://iopscience.iop.org/article/10.7452/lapl.201210041/pdf

[14] Y. H. Park, D. Won Lee, H. J. Kong, and Y. S. Kim, "Cavity-dumped 2.70 µm erbium laser using optomechanical shutter," *Review of Scientific Instruments*, vol. 79, no. 12, p. 123102, 2008. [Online]. Available: http://www.ncbi.nlm.nih.gov/pubmed/19123540http://aip.scitation.org/doi/10.1063/1.3036976

[15] J. Zayhowski, "Q-switched microchip lasers find real-world application," *Laser focus world*, vol. 35, no. 8, pp. 129–136, 1999. [Online]. Available: http://cat.inist.fr/?aModele=afficheN&cpsidt=1181847

[16] J. M. Serres, V. Jambunathan, X. Mateos, P. Loiko, A. Lucianetti, T. Mocek, K. Yumashev, V. Petrov, U. Griebner, M. Aguilo, and F. Diaz, "Graphene Q-switched compact Yb:YAG laser," *IEEE Photonics Journal*, vol. 7, no. 5, pp. 1–7, 2015. [Online]. Available: http://ieeexplore.ieee.org/document/7239523/

[17] H. Tanaka, R. Kariyama, K. Iijima, K. Hirosawa, and F. Kannari, "Saturation of 640-nm absorption in Cr4+:YAG for an InGaN laser diode pumped passively Q-switched Pr3+:YLF laser," *Optics Express*, vol. 23, no. 15, p. 19382, 2015. [Online]. Available: https://www.osapublishing.org/abstract.cfm?URI=oe-23-15-19382

[18] A. Siegman, *Lasers*. University Science Books, 1986.

[19] W. E. Lamb, "Theory of an Optical Maser," *Physical Review*, vol. 134, no. 6A, pp. A1429–A1450, 1964. [Online]. Available: https://link.aps.org/doi/10.1103/PhysRev.134.A1429

[20] L. E. Hargrove, R. L. Fork, and M. A. Pollack, "Locking of He-Ne laser modes induced by synchronous intracavity modulation," *Applied Physics Letters*, vol. 5, no. 1, pp. 4–5, 1964. [Online]. Available: http://aip.scitation.org/doi/10.1063/1.1754025

[21] H. Haus, "Mode-locking of lasers," *IEEE Journal of Selected Topics in Quantum Electronics*, vol. 6, no. 6, pp. 1173–1185, 2000. [Online]. Available: http://ieeexplore.ieee.org/document/902165/

[22] I. Martial, F. Balembois, J. Didierjean, and P. Georges, "Nd:YAG single-crystal fiber as high peak power amplifier of pulses below one nanosecond," *Optics Express*, vol. 19, no. 12, pp. 900–909, 2011.

[23] P. Russbueldt, D. Hoffmann, M. Höfer, J. Löhring, J. Luttmann, A. Meissner, J. Weitenberg, M. Traub, T. Sartorius, D. Esser, R. Wester, P. Loosen, and R. Poprawe, "Innoslab amplifiers," *IEEE Journal on Selected Topics in Quantum Electronics*, vol. 21, no. 1, 2015.

[24] Teollisuuden Voima Oyj, "Nuclear power plant unit: Olkiluoto 3," 2017. [Online]. Available: http://www.tvo.fi/uploads/julkaisut/tiedostot/ydinvoimalayks_OL3_ENG.pdf

[25] A. Klehr, A. Liero, T. Hoffann, S. Schwertfeger, G. Erbert, W. Heinrich, and G. Trankle, "A new concept of an ultra fast pulse picker for fs- and ps-pulses from GHz pulse-trains with semiconductor tapered elements," in *CLEO/Europe - EQEC 2009 - European Conference on Lasers and Electro-Optics and the European Quantum Electronics Conference*. IEEE, 2009, pp. 1–1. [Online]. Available: http://ieeexplore.ieee.org/document/5194823/

[26] J.-P. Ruske, E. Werner, B. Zeitner, and A. Tunnermann, "Integrated optical ultrashort-pulse picker with high extinction ratio," *Electronics Letters*, vol. 39, no. 20, p. 1442, 2003. [Online]. Available: http://digital-library.theiet.org/content/journals/10.1049/el_20030959

[27] J. E. Murray and W. H. Lowdermilk, "ND:YAG regenerative amplifier," *Journal of Applied Physics*, vol. 51, no. 7, pp. 3548–3556, 1980. [Online]. Available: http://aip.scitation.org/doi/10.1063/1.328194

[28] M. Grishin, V. Gulbinas, and A. Michailovas, "Dynamics of high repetition rate regenerative amplifiers," *Optics Express*, vol. 15, no. 15, p. 9434, 2007. [Online]. Available: https://www.osapublishing.org/oe/abstract.cfm?uri=oe-15-15-9434

[29] I. Nissinen, A. K. Lansman, J. Nissinen, J. Holma, and J. Kostamovaara, "2x(4x)128 time-gated CMOS single photon avalanche diode line detector with 100 ps resolution for Raman spectroscopy," *European Solid-State Circuits Conference*, pp. 291–294, 2013.

[30] J. Kostamovaara, J. Tenhunen, M. Kögler, I. Nissinen, J. Nissinen, and P. Keränen, "Fluorescence suppression in Raman spectroscopy using a time-gated CMOS SPAD," *Optics Express*, vol. 21, no. 25, p. 31632, 2013. [Online]. Available: https://www.osapublishing.org/oe/abstract.cfm?uri=oe-21-25-31632

[31] C.-L. Lin, G. Vitrant, M. Bouriau, R. Casalegno, and P. L. Baldeck, "Optically driven Archimedes micro-screws for micropump application," *Optics Express*, vol. 19, no. 9, p. 8267, 2011. [Online]. Available: https://www.osapublishing.org/abstract.cfm?URI=oe-19-9-8267

[32] B. S. Haq, H. U. Khan, I. Zari, K. Alam, M. Mateenullah, and S. Attaullah, "Study of the two-photon excitation of photoinitiator in various solvents, and the two-photon polymerization process," *Applied Optics, Vol. 54, Issue 23, pp. 7020-7026*, vol. 54, no. 23, pp. 7020–7026, 2015. [Online]. Available: https://www.osapublishing.org/ao/abstract.cfm?uri=ao-54-23-7020&origin=search

[33] A. Periasamy, P. Wodnicki, X. F. Wang, S. Kwon, G. W. Gordon, and B. Herman, "Time-resolved fluorescence lifetime imaging microscopy using a picosecond pulsed tunable dye laser system," *Review of Scientific Instruments*, vol. 67, no. 10, pp. 3722–3731, 1996. [Online]. Available: http://aip.scitation.org/doi/10.1063/1.1147139

[34] S. W. Hell and J. Wichmann, "Breaking the diffraction resolution limit by stimulated emission: stimulated-emission-depletion fluorescence microscopy," *Optics Letters*, vol. 19, no. 11, p. 780, 1994. [Online]. Available: https://www.osapublishing.org/abstract.cfm?URI=ol-19-11-780

[35] P. Schulze, M. Ludwig, and D. Belder, "Impact of laser excitation intensity on deep UV fluorescence detection in microchip electrophoresis," *Electrophoresis*, vol. 29, no. 24, pp. 4894–4899, 2008.

[36] R. Paschotta, *Encyclopedia of laser physics and technology*, 1st ed. Wiley-vch Berlin, 2008.

[37] B. E. A. Saleh and M. C. Teich, *Fundamentals of Photonics*, ser. Wiley Series in Pure and Applied Optics. New York, USA: John Wiley & Sons, Inc., 1991. [Online]. Available: http://doi.wiley.com/10.1002/0471213748

[38] R. W. Hellwarth, "Theory of the pulsation of fluorescent light from ruby," *Physical Review Letters*, vol. 6, no. 1, pp. 9–12, 1961.

[39] F. J. McClung and R. W. Hellwarth, "Giant pulsations from ruby," *Bull. Am. Phys. Soc.*, vol. 6, p. 414, 1961.

[40] W. G. Wagner and B. A. Lengyel, "Evolution of the giant pulse in a laser," *Journal of Applied Physics*, vol. 34, no. 7, pp. 2040–2046, 1963.

[41] L. E. Erickson and A. Szabo, "Effects of saturable absorber lifetime on the performance of giant-pulse lasers," *Journal of Applied Physics*, vol. 37, no. 13, pp. 4953–4961, 1966. [Online]. Available: http://aip.scitation.org/doi/10.1063/1.1708172

[42] ———, "Behavior of saturable-absorber giant-pulse lasers in the limit of large absorber cross section," *Journal of Applied Physics*, vol. 38, no. 6, pp. 2540–2542, 1967. [Online]. Available: http://aip.scitation.org/doi/10.1063/1.1709945

[43] G. J. Spühler, R. Paschotta, R. Fluck, B. Braun, M. Moser, G. Zhang, E. Gini, and U. Keller, "Experimentally confirmed design guidelines for passively Q-switched microchip lasers using semiconductor saturable absorbers," *Journal of the Optical Society of America B*, vol. 16, no. 3, p. 376, 1999. [Online]. Available: https://www.osapublishing.org/abstract.cfm?URI=josab-16-3-376

[44] A. C. Butler, D. J. Spence, and D. W. Coutts, "Scaling Q-switched microchip lasers for shortest pulses," *Applied Physics B*, vol. 109, no. 1, pp. 81–88, 2012. [Online]. Available: http://link.springer.com/10.1007/s00340-012-5223-2

[45] E. Mehner, B. Bernard, H. Giessen, D. Kopf, and B. Braun, "Sub-20-ps pulses from a passively Q-switched microchip laser at 1 MHz repetition rate," *Optics Letters*, vol. 39, no. 10, p. 2940, 2014. [Online]. Available: http://dx.doi.org/10.1364/OL.39.002940https://www.osapublishing.org/abstract.cfm?URI=ol-39-10-2940

[46] J. J. Zayhowski and A. Mooradian, "Single-frequency microchip Nd lasers," *Optics Letters*, vol. 14, no. 1, 1989.

[47] J. Zayhowski, "Microchip lasers," *The Lincoln Laboratory Journal*, vol. 3, no. 3, pp. 427–446, 1990.

[48] J. Dong, K.-I. Ueda, A. Shirakawa, H. Yagi, T. Yanagitani, and A. Kaminskii, "Composite Yb:YAG/Cr(4+):YAG ceramics picosecond microchip lasers." *Optics Express*, vol. 15, no. 22, pp. 14 516–14 523, 2007. [Online]. Available: http://www.ncbi.nlm.nih.gov/pubmed/19550730

[49] J. Dong, K.-i. Ueda, H. Yagi, and A. A. Kaminskii, "Laser-diode pumped self-Q-switched microchip lasers," *Optical Review*, vol. 15, no. 2, pp. 57–74, 2008. [Online]. Available: http://link.springer.com/10.1007/s10043-008-0010-3

[50] U. Keller, K. J. Weingarten, F. X. Kärtner, D. Kopf, B. Braun, I. D. Jung, R. Fluck, C. Hönninger, N. Matuschek, and J. Aus der Au, "Semiconductor saturable absorber mirrors (SESAM's) for femtosecond to nanosecond pulse generation in solid-state lasers," *IEEE Journal of Selected Topics in Quantum Electronics*, vol. 2, no. 3, pp. 435–453, 1996. [Online]. Available: http://ieeexplore.ieee.org/lpdocs/epic03/wrapper.htm?arnumber=571743

[51] L. Orsila, A. Härkönen, J. Hyyti, M. Guina, and G. Steinmeyer, "Ultrahigh precision nonlinear reflectivity measurement system for saturable absorber mirrors with self-referenced fluence characterization," *Optics Letters*, vol. 39, no. 15, p. 4384, 2014. [Online]. Available: http://www.opticsinfobase.org/abstract.cfm?URI=ol-39-15-4384

[52] C. J. Saraceno, C. Schriber, M. Mangold, M. Hoffmann, O. H. Heckl, C. R. E. Baer, M. Golling, T. Sudmeyer, and U. Keller, "SESAMs for high power oscillators: Damage thresholds and design guidelines," *CLEO: 2011 - Laser Science to Photonic Applications*, vol. 18, no. 1, pp. 1–2, 2011.

[53] A. W. Tucker, M. Birnbaum, C. L. Fincher, and J. W. Erler, "Stimulated-emission cross section at 1064 and 1342 nm in Nd:YVO4," *Journal of Applied Physics*, vol. 48, no. 12, pp. 4907–4911, 1977. [Online]. Available: http://aip.scitation.org/doi/10.1063/1.323618

[54] O. Kimmelma, I. Tittonen, and S. C. Buchter, "Thermal tuning of laser pulse parameters in passively Q-switched Nd:YAG lasers." *Applied Optics*, vol. 47, no. 23, pp. 4262–4266, 2008. [Online]. Available: http://www.ncbi.nlm.nih.gov/pubmed/18690268

[55] X. Délen, F. Balembois, and P. Georges, "Temperature dependence of the emission cross section of Nd:YVO4 around 1064 nm and consequences on laser operation," *Journal of the Optical Society of America B: Optical Physics*, vol. 28, no. 5, pp. 972–976, 2011. [Online]. Available: http://josab.osa.org/abstract.cfm?URI=josab-28-5-972

[56] Q. Mingxin, D. J. Booth, G. W. Baxter, and G. C. Bowkett, "Performance of a Nd:YVO4 microchip laser with continuous-wave pumping at wavelengths between 741 and 825 nm." *Applied optics*, vol. 32, no. 12, pp. 2085–6, 1993. [Online]. Available: http://www.ncbi.nlm.nih.gov/pubmed/20820348

[57] Y. Sato and T. Taira, "Highly accurate interferometric evaluation of thermal expansion and dn/dT of optical materials," *Optical Materials Express*, vol. 4, no. 5, p. 876, 2014. [Online]. Available: https://www.osapublishing.org/ome/abstract.cfm?uri=ome-4-5-876

[58] J. Didierjean, E. Herault, F. Balembois, and P. Georges, "Thermal conductivity measurements of laser crystals by infrared thermography. Application to Nd:doped crystals," *Optics Express*, vol. 16, no. 12, p. 8995, 2008. [Online]. Available: https://www.osapublishing.org/oe/abstract.cfm?uri=oe-16-12-8995

[59] R. O. Carlson, G. A. Slack, and S. J. Silverman, "Thermal conductivity of GaAs and GaAs1-xPx laser semiconductors," *Journal of Applied Physics*, vol. 36, no. 2, pp. 505–507, 1965. [Online]. Available: http://aip.scitation.org/doi/10.1063/1.1714018

[60] U. Keller, "Recent developments in compact ultrafast lasers," *Nature*, vol. 424, no. 6950, pp. 831–838, 2003. [Online]. Available: http://www.nature.com/doifinder/10.1038/nature01938

[61] R. W. Boyd, *Nonlinear Optics*, 2nd ed. Academic Press, 2003.

[62] M. Bass, *Handbook of Optics, Volume 2*, 2nd ed. McGraw-Hill Professional, 1994.

[63] C. V. Raman and K. S. Krishnan, "A new type of secondary radiation," *Nature*, vol. 121, no. 3048, pp. 501–502, 1928.

[64] Y. R. Shen and N. Bloembergen, "Theory of stimulated brillouin and raman scattering," *Physical Review*, vol. 137, no. 6A, 1965.

[65] A. Penzkofer, A. Laubereau, and W. Kaiser, *High intensity Raman interactions*, 1st ed. Oxford, New York : Pergamon Press, 1979. [Online]. Available: http://trove.nla.gov.au/work/26811037

[66] W. Lubeigt, G. M. Bonner, J. E. Hastie, M. D. Dawson, D. Burns, and A. J. Kemp, "Continuous-wave diamond Raman laser," *Optics letters*, vol. 35, no. 17, pp. 2994–2996, 2010.

[67] O. Kitzler, A. McKay, and R. P. Mildren, "Continuous-wave wavelength conversion for high-power applications using an external cavity diamond Raman laser," *Optics Letters*, vol. 37, no. 14, p. 2790, 2012.

[68] D. J. Spence, E. Granados, and R. P. Mildren, "Mode-locked picosecond diamond Raman laser," *Optics letters*, vol. 35, no. 4, pp. 556–558, 2010.

[69] R. P. Mildren, A. Sabella, E. Granados, and D. J. Spence, "Diamond Raman lasers," *Osa Cleo Qels*, pp. 573–574, 2010.

[70] R. P. Mildren, J. E. Butler, and J. R. Rabeau, "CVD-diamond external cavity Raman laser at 573 nm," *Optics express*, vol. 16, no. 23, pp. 18 950–18 955, 2008.

[71] S. Reilly, V. G. Savitski, H. Liu, E. Gu, M. D. Dawson, and A. J. Kemp, "Monolithic diamond Raman laser," *Optics Letters*, vol. 40, no. 6, p. 930, 2015. [Online]. Available: http://ol.osa.org/abstract.cfm?URI=ol-40-6-930

[72] P. Cerny, H. Jelinkova, T. Basiev, and P. Zverev, "Highly efficient picosecond Raman generators based on the BaWO crystal in the near infrared, visible, and ultraviolet," *IEEE Journal of Quantum Electronics*, vol. 38, no. 11, pp. 1471–1478, 2002.

[73] T. T. Basiev, P. G. Zverev, A. Y. Karasik, V. V. Osiko, A. A. Sobol', and D. S. Chunaev, "Picosecond stimulated Raman scattering in crystals," *Journal of Experimental and Theoretical Physics*, vol. 99, no. 5, pp. 934–941, 2004. [Online]. Available: http://link.springer.com/10.1134/1.1842874

[74] W. Lubeigt, G. M. Bonner, J. E. Hastie, M. D. Dawson, D. Burns, and A. J. Kemp, "An intra-cavity Raman laser using synthetic single-crystal diamond," *Optics express*, vol. 18, no. 16, pp. 16 765 – 16 770, 2010.

[75] S. V. Voitikov, A. A. Demidovich, A. S. Grabtchikov, P. V. Shpak, M. B. Danailov, and V. A. Orlovich, "Two-Stokes generation and effect of multiwave mixing on output pulse parameters of a Q-switched Raman microchip laser," *Journal of the Optical Society of America B*, vol. 27, no. 6, pp. 1232 – 1241, 2010. [Online]. Available: http://www.opticsinfobase.org/abstract.cfm?URI=josab-27-6-1232

[76] S. Ding, X. Zhang, Q. Wang, F. Su, S. Li, S. Fan, S. Zhang, J. Chang, S. Wang, and Y. Liu, "Theoretical models for the extracavity Raman laser with crystalline Raman medium," *Applied Physics B*, vol. 85, no. 1, pp. 89 – 95, 2006. [Online]. Available: http://link.springer.com/10.1007/s00340-006-2306-y

[77] R. P. Mildren and J. Rabeau, *Optical engineering of diamond*, 1st ed. Wiley-VCH, 2013.

[78] V. G. Savitski, S. Reilly, and A. J. Kemp, "Steady-state raman gain in diamond as a function of pump wavelength," *IEEE Journal of Quantum Electronics*, vol. 49, no. 2, pp. 218 – 223, 2013. [Online]. Available: http://ieeexplore.ieee.org/document/6401143/

[79] Y. Jeong, J. K. Sahu, D. N. Payne, and J. Nilsson, "Ytterbium-doped large-core fiber laser with 1 kW continuous-wave output power," *Advanced Solid-State Photonics*, p. PDP13, 2004. [Online]. Available: https://www.osapublishing.org/abstract.cfm?uri=ASSP-2004-PDP13

[80] X. Shen, H. Zhang, H. Hao, D. Li, P. Yan, and M. Gong, "Self-phase modulation of nanosecond pulses in fiber amplifiers with gain saturation," *Optics Express*, vol. 24, no. 5, p. 4382, 2016. [Online]. Available: https://www.osapublishing.org/abstract.cfm?URI=oe-24-5-4382

[81] G. Wang, D. Chen, Y. Cheng, and J. Dong, "Yb:YAG enhanced Cr,Yb:YAG self-Q-switched microchip laser under QCW laser-diode pumping," *Optics and Laser Technology*, vol. 68, pp. 136 – 140, 2015. [Online]. Available: http://dx.doi.org/10.1016/j.optlastec.2014.11.020

[82] Y. Zaouter, I. Martial, X. Délen, N. Aubry, C. Hönninger, E. Mottay, P. Georges, and F. Druon, "12 W, 350 fs ultrashort pulses from a micro-pulling down Yb:YAG single crystal fiber amplifier," *The European Conference on Lasers and Electro-Optics*, vol. 207, no. 2008, p. 3495, 2009.

[83] F. Lesparre, J. T. Gomes, X. Délen, I. Martial, J. Didierjean, W. Pallmann, B. Resan, F. Druon, F. Balembois, and P. Georges, "Yb:YAG single-crystal fiber amplifiers for picosecond lasers using the divided pulse amplification technique," *Opt. Lett.*, vol. 41, no. 7, pp. 1628 – 1631, 2016. [Online]. Available: https://www.osapublishing.org/ol/abstract.cfm?uri=ol-41-7-1628

[84] P. Russbueldt, T. Mans, G. Rotarius, and J. Weitenberg, "400 W Yb:YAG Innoslab fs-amplifier," *Optics Letters*, vol. 17, no. 15, pp. 1013 – 1023, 2009.

[85] Y.-h. Cha, K.-h. Ko, G. Lim, and J.-m. Han, "External-cavity frequency doubling of a 5-W 756-nm injection-locked Ti:sapphire laser," *Optics Express*, vol. 16, no. 7, pp. 4866 – 4871, 2008.

[86] A. Agnesi, L. Carra, F. Pirzio, G. Reali, A. Tomaselli, D. Scarpa, and C. Vacchi, "Amplification of a low-power picosecond Nd:YVO4 laser by a diode-laser side-pumped grazing-incidence slab amplifier," *IEEE Journal of Quantum Electronics*, vol. 42, no. 8, pp. 772 – 776, 2006. [Online]. Available: http://ieeexplore.ieee.org/document/1658128/

Tampereen teknillinen yliopisto
PL 527
33101 Tampere

Tampere University of Technology
P.O.B. 527
FI-33101 Tampere, Finland

ISBN 978-952-15-4047-9
ISSN 1459-2045